Macroscopic Modelling of Flow-Drill Screw Connections in Thin-Walled Aluminium Structures

Johan Kolstø Sønstabø[a,b,*], David Morin[a,b], Magnus Langseth[a,b]

[a] *Centre for Advanced Structural Analysis (CASA), Norwegian University of Science and Technology (NTNU), NO-7491 Trondheim, Norway*
[b] *Structural Impact Laboratory (SIMLab), Department of Structural Engineering, Norwegian University of Science and Technology (NTNU), NO-7491 Trondheim, Norway*

Abstract

This paper presents an investigation on the modelling of flow-drill screw connections in thin-walled aluminium plates in large-scale finite element analyses using different macroscopic modelling techniques. Five models that were originally developed for adhesive bonds, spot welds and self-piercing rivet connections were examined. Two sets of experimental data were used, each with a different screw and material combination. Different trends were observed for the two sets, which challenged the flexibility of the models. The results indicated that a constraint-based model originally developed for self-piercing rivet connections was the best suited model. A two-step validation strategy was proposed and used for the present models.

Keywords: Flow-drill screw, Connection, Finite element, Large-scale, Automotive, Macroscopic

1. Introduction

Joining with flow-drill screws (FDS) is a common technique for joining dissimilar materials in the load-bearing structure of cars. Under impact loadings, the behaviour and fracture of connections are important for the response of the thin-walled structure. In the automotive industry, large-scale finite element (FE) simulations with shell elements (for instance, crash simulations) are extensively used in the vehicle design process, and accurate modelling of connections plays an important role in obtaining reliable predictive results. Due to time step limitations, the physical geometry of connections and potential process effects cannot be modelled; rather, simplified models are necessary to represent the connections. These models should be capable of describing the macroscopic response while being computationally efficient.

Several different approaches have been used for different connection types, and various models have been designed for, e.g., spot welds, adhesives and self-piercing rivet connections. However, no models have been specifically developed for modelling FDS connections. Furthermore, no reports regarding the modelling of FDS connections have been found in the available literature. The aim of this study was to assess the ability of existing macroscopic

*Corresponding author
Email address: johan.k.sonstabo@ntnu.no (Johan Kolstø Sønstabø)

connection models to represent FDS connections. Different strategies for connection modelling are presented in the following.

One of the simplest approaches is to assign a rigid link between two nodes on opposing shell surfaces (Fig. 1a). However, this approach requires the nodes to be aligned, which is an exhausting restriction for large-scale analyses, and with this approach, the local deformation behaviour of the connection cannot be taken into account. An easier approach is to use a beam element for the connection attached to the surfaces with tie constraints (Fig. 1b). Then, deformation behaviour may be accounted for, but this approach has been shown to be mesh dependent, as noted by Malcolm and Nutwell (2007), who used a material model designed for spot welds in the beams. A drawback of this method is that the time step may be limited by the beam length. Another method is to use one or several hexahedral elements in an assembly to represent a connection (Figs. 1c and 1d), and this method has been shown to be mesh independent if eight or more elements are included in the assembly (Malcolm and Nutwell, 2007). However, refining the connection mesh might decrease the time step. To predict accurate responses, different material models can be assigned to these clusters of elements. Such models are herein referred to as *element-based* models.

Element-based models are commonly used for modelling of structural bonds (e.g. Yamashita et al. (2013)). In some part configurations structural bonding and discrete connections (such as FDS connections) are commonly combined. A way to model such hybrid joints is to use an element-based model for the adhesive bond, in combination with a discrete model for the discrete connections (e.g. Carlberger and Stigh (2010)).

A material model designed to predict spot weld failure was presented by Hallquist et al. (2007), under the name *mat spotweld*. This model is an elastic-plastic model with isotropic linear hardening coupled with different failure models. Seeger et al. (2005) showed that this model could realistically describe spot welds using either a single beam element, a single hexahedron element or four hexahedron elements to represent the connection (see Figs. 1b, 1c and 1d). These authors argued that using four hexahedron elements was too expensive because it limited the simulation time step. Bier et al. (2010) evaluated the ability of the cohesive element model presented by Marzi et al. (2009) to represent spot welds (this model is available in the FE software LS-DYNA under the name *mat cohesive mixed mode elastoplastic rate* (Hallquist et al., 2007)). It was compared to *mat spotweld*, and they found that the model of Marzi et al. (2009) was beneficial for some load cases. They obtained better results with a cluster of four or eight elements rather than with a single element.

A model tailored for self-piercing rivet connections was reported by Hanssen et al. (2010) (available in LS-DYNA as the model *constrained spr2* (Hallquist et al., 2007)). This is a *constraint-based* model, which means that the connection is represented by a constraint formulation rather than by an assembly of elements (Fig. 1e). Tensile and shear behaviours are uncoupled, and damage is taken into account. They defined a strong coupling between mode mixity and damage evolution based on experimental observations. It was shown that mesh dependency was limited and that the model was well suited for self-piercing rivet connections.

Another constraint-based model (named *constrained interpolation spotweld* (model 1 in LS-DYNA®) by Hallquist et al. (2007)) was developed for spot welds. In this model, tensile and shear behaviours are coupled through a

plasticity-like formulation.

Sommer and Maier (2008) investigated the abilities of *mat spotweld*, the model *mat arup adhesive* (Hallquist et al., 2007), the element-based model of Marzi et al. (2009), the constraint-based model of Hanssen et al. (2010), and *constrained interpolation spotweld* to represent self-piercing rivet connections. They found that the model of Marzi et al. (2009) was the most promising and that *mat spotweld* was the least promising. However, they noted that the model proposed by Marzi et al. (2009) was insufficient under peeling loadings and that it had no flexibility to control the mixed-mode behaviour. The model *mat arup adhesive* is a cohesive zone model with linear elasticity and damage (no plasticity), which is too simple for FDS connections, and therefore, this model is not included in the present study.

Further modifications to *constrained interpolation spotweld* were presented by Bier and Sommer (2013), and they showed that the ability to model self-piercing rivet connections was enhanced (this model is availbale in LS-DYNA® as *constrained interpolation spotweld* (model 2)).

When calibrating macroscopic models, it is important to have a proper strategy for validation. The model should be calibrated to tests under controlled loading paths and validated to tests with different and more complex loadings. Hoang et al. (2012) used U-shaped specimens under controlled tensile, combined tensile and shear, and shear loadings for calibration and validated the model using a complex component test (T-component). Similarly, Bier and Sommer (2013) used KSII tests for calibration and a complex component (T-joint) test for validation.

In this work, the ability of five common state-of-the-art connection models to represent FDS connections was studied. The examined models were the element-based *mat spotweld*, the element-based model by Marzi et al. (2009), the constraint-based model by Hanssen et al. (2010) and the two versions of the constraint-based model *constrained interpolation spotweld*. These models were calibrated to experimental data from two different connections with different screw and material combinations. A thorough two-step procedure for validation is presented and used.

2. Experiments

Here, the term *connection* is based on the definition of Sønstabø et al. (2015), i.e., *a system that mechanically fastens two or more parts together*. Thus, a connection consists of a screw and surrounding plate material (see Fig. 2). In the first set of experiments, a short screw with a nominal length of 10 mm, a nominal shaft diameter of 4 mm and a nominal head diameter of 8 mm joined two aluminium sheets (alloy 6016 T4), while in the second set of experiments, a long screw with a nominal length of 30 mm, a nominal shaft diameter of 5 mm and a nominal head diameter of 14 mm joined an aluminium sheet (alloy 6016 T4) to an aluminium extrusion (alloy 6063 T6). The nominal thicknesses of the sheet and extrusion were 2 mm. A pre-hole was used in the top plate for both connections. The two connections are hereafter denoted as the *small screw connection* and the *large screw connection*, respectively. Each set of experiments consisted of cross tests in three loading directions (tension, shear and combined tension and shear), single lap joint and peeling tests, and T-component tests.

An extensive study of the behaviour of the small screw connection has previously been reported by Sønstabø et al.

(2015), which included cross, single lap joint and peeling tests. Using the same experimental set-up, corresponding tests were conducted in this work for the large screw connection. Drawings of the specimens with their nominal dimensions are presented in Fig. 3. The cross specimens (Fig. 3a) were identical for the two connections, whereas there were some differences for the single lap joint (Figs. 3b and 3d) and peeling specimens (Figs. 3c and 3e). The cross-head force and displacement were measured during the tests.

In addition to the single-connector tests, T-component tests were performed. The T-component specimens consisted of a hat-shaped sheet joined to a U-shaped sheet/extrusion. Drawings of the specimens with their nominal dimensions are presented in Figs. 4a and 4b. The test set-up was adopted from Hoang et al. (2012). Pictures of the test rig are presented in Figs. 4c and 4d. As shown, the U-shaped part was clamped at both ends, and the load was applied in the longitudinal direction of the hat-shaped part. Three-dimensional digital image correlation was used as a virtual extensometer, measuring the relative displacement between the sheets by tracking one point on each part, as illustrated with yellow dots in Fig. 4e.

Force-displacement curves from the single lap joint tests are presented along with the simulation results in Section 5. However, selected results from the cross, peeling and T-component tests are included here to highlight the differences observed between the two connections, which were significant for the present study.

Representative curves from the cross tests are presented in Fig. 5. As shown, when going from shear to mixed and tensile loading, the maximum load decreased and the displacement at maximum load increased for both connections. However, for the displacement at failure, the trend differed for the two connections. For the small screw connection, the displacement at failure increased when going from shear to mixed and tensile loading, whereas it decreased for the large screw connection. It was also observed that the macroscopic behaviour in mixed mode appears to be very different for the two connections.

Fig. 6 presents representative curves from the peeling tests. The difference between the two connections is the increased slope observed for the large screw connection just before the maximum load (at approximately 23 mm). This was an effect of contact between the tail of the screw and the plate material. Tail contact did not occur for the small screw connection due to the shorter length of the screw.

Force-displacement curves from the T-component tests are presented in Fig. 7. All repetitions are included because some scatter was evident. As shown in this figure, the behaviour after the maximum force differed for the two connections. For the small screw connection, failure occurred almost immediately after the maximum force was reached, without any softening. For the large screw connection, however, significant softening was observed before failure occurred. Moreover, the sudden failure that occurred for both connections differed from the failure observed in the cross shear tests, which might indicate that the failure mechanisms at the component level differ from those observed in the single-connector tests. This result was observed in the study of Sønstabø et al. (2015) when comparing axial crushing tests to cross tests for the small screw connection.

The differences discussed herein indicate that a high level of model flexibility is required for a macroscopic connection model to represent the behaviours of both connections.

3. Modelling of plate materials

To minimise the uncertainty linked to the plate material when modelling connections, an advanced rate-independent hypoelastic-plastic material model was applied for the rolled sheet in alloy 6016 temper T4 and the extrusion in alloy 6063 temper T6. An anisotropic yield surface was used, the associated flow rule was assumed, and isotropic work hardening was applied. Kinematic hardening was not considered because the loadings were assumed to be monotonic.

Material tests were performed to characterise the materials. One set of material tests (uniaxial tensile tests and disk compression tests) was used to calibrate the yield surface and hardening parameters. Plane strain tension and in-plane single shear tests were used to validate the material models because they challenge other parts of the yield surface.

In the following section, the material model and the calibration/validation procedure are presented.

3.1. Material model

Because rolled and extruded alloys typically exhibit significant plastic anisotropy (Lademo et al., 1999), the 18-parameter anisotropic yield function Yld2004-18p (Barlat et al., 2005) was selected to describe the yielding and the plastic flow of the aluminium plates. This yield surface was chosen for its flexibility to cover a wide range of aluminium textures. It is constructed by two linear transformations of the deviatoric stress tensor, where the two transformation tensors include a total of 18 independent coefficients that weight the components of the deviatoric stress tensor to account for plastic anisotropy. In addition, the function includes an exponent m that determines the curvature. With the yield function

$$f = \phi - (\sigma_0 + R) \leq 0,$$

where σ_0 is the yield stress and R is an isotropic hardening variable, Barlat et al. (2005) proposed the function ϕ, as follows,

$$\begin{aligned} 4\phi^m = &\left|\tilde{S}'_1 - \tilde{S}''_1\right|^m + \left|\tilde{S}'_1 - \tilde{S}''_2\right|^m + \left|\tilde{S}'_1 - \tilde{S}''_3\right|^m \\ &+ \left|\tilde{S}'_2 - \tilde{S}''_1\right|^m + \left|\tilde{S}'_2 - \tilde{S}''_2\right|^m + \left|\tilde{S}'_2 - \tilde{S}''_3\right|^m \\ &+ \left|\tilde{S}'_3 - \tilde{S}''_1\right|^m + \left|\tilde{S}'_3 - \tilde{S}''_2\right|^m + \left|\tilde{S}'_3 - \tilde{S}''_3\right|^m. \end{aligned}$$

Here, $\tilde{S}'_1$, $\tilde{S}'_2$, $\tilde{S}'_3$ and $\tilde{S}''_1$, $\tilde{S}''_2$, $\tilde{S}''_3$ are the principal values of the tensors $\tilde{\mathbf{s}}'$ and $\tilde{\mathbf{s}}''$, respectively, which are defined through the transformations

$$\begin{aligned} \tilde{\mathbf{s}}' &= \mathbf{C}' \cdot \mathbf{s} \\ \tilde{\mathbf{s}}'' &= \mathbf{C}'' \cdot \mathbf{s}, \end{aligned}$$

where $\mathbf{s}$ is the deviatoric part of the Cauchy stress tensor. The transformation tensors $\mathbf{C}'$ and $\mathbf{C}''$ each contain nine independent coefficients. If $\mathbf{s}$ is expressed in matrix form using Voigt notation, the transformation tensors may be

expressed in matrix form as

$$\boldsymbol{C}' = \begin{bmatrix} 0 & -c'_{12} & -c'_{13} & 0 & 0 & 0 \\ -c'_{21} & 0 & -c'_{23} & 0 & 0 & 0 \\ -c'_{31} & -c'_{32} & 0 & 0 & 0 & 0 \\ 0 & 0 & 0 & -c'_{44} & 0 & 0 \\ 0 & 0 & 0 & 0 & -c'_{55} & 0 \\ 0 & 0 & 0 & 0 & 0 & -c'_{66} \end{bmatrix}$$

$$\boldsymbol{C}'' = \begin{bmatrix} 0 & -c''_{12} & -c''_{13} & 0 & 0 & 0 \\ -c''_{21} & 0 & -c''_{23} & 0 & 0 & 0 \\ -c''_{31} & -c''_{32} & 0 & 0 & 0 & 0 \\ 0 & 0 & 0 & -c''_{44} & 0 & 0 \\ 0 & 0 & 0 & 0 & -c''_{55} & 0 \\ 0 & 0 & 0 & 0 & 0 & -c''_{66} \end{bmatrix}.$$

The 18 coefficients have no physical meaning and must be determined by using optimisation methods.

To represent isotropic work hardening, the Voce hardening law was used. With the Voce law, the isotropic hardening variable R is

$$R = \sum_{i=1}^{N_R} Q_{Ri} \left(1 - \exp\left(-\frac{\theta_{Ri}}{Q_{Ri}} p \right) \right), \tag{1}$$

where p is the equivalent plastic strain, N_R is the number of terms, and Q_{Ri} and θ_{Ri} are the saturation value and initial hardening moduli for term i, respectively. Three terms were required for the sheet, whereas two terms were sufficient for the extrusion material.

3.2. Calibration of material model

To determine the shape of the yield surface, uniaxial tensile tests were performed in seven material directions (0°, 15°, 30°, 45°, 60°, 75° and 90° to the rolling/extrusion direction), and disk compression tests (coin tests) were performed.

For each tensile test, the flow stress ratio (r-ratio), which is defined as

$$r_\alpha(W^\mathrm{p}) = \left. \frac{\sigma_\alpha}{\sigma_\mathrm{ref}} \right|_{W^\mathrm{p}}, \tag{2}$$

was calculated. In (2), σ_α and σ_ref are the flow stresses in the α and reference directions, respectively, and W^p is the amount of plastic work. The rolling/extrusion direction was chosen as the reference direction. An average r-ratio was calculated for each test as follows,

$$r_\alpha^\mathrm{avg} = \frac{1}{W^\mathrm{p}_\mathrm{max}} \int_0^{W^\mathrm{p}_\mathrm{max}} r_\alpha(W^\mathrm{p}) \mathrm{d}W^\mathrm{p},$$

where $W^{\mathrm{p}}_{\max}$ is the amount of plastic work at the onset of diffuse necking.

The plastic strain ratio (R-ratio), which is defined as

$$R_\alpha = \left.\frac{\dot{\varepsilon}^{\mathrm{p}}_{\mathrm{w}}}{\dot{\varepsilon}^{\mathrm{p}}_{\mathrm{t}}}\right|_\alpha \approx \left.\frac{\varepsilon^{\mathrm{p}}_{\mathrm{w}}}{\varepsilon^{\mathrm{p}}_{\mathrm{t}}}\right|_\alpha, \tag{3}$$

was calculated from measurements of the specimen cross-sections before and after the uniaxial tensile tests. In (3), $\dot{\varepsilon}^{\mathrm{p}}_{\mathrm{w}}$ and $\dot{\varepsilon}^{\mathrm{p}}_{\mathrm{t}}$ are the plastic strain rates in the width and thickness directions, respectively, and $\varepsilon^{\mathrm{p}}_{\mathrm{w}}$ and $\varepsilon^{\mathrm{p}}_{\mathrm{t}}$ are the corresponding plastic strains during the uniaxial tensile tests, obtained from thickness and width measurements of the tensile specimens before and after the tests.

The gradient of the yield surface in equi-biaxial tension was determined using coin tests, in which a circular disk is compressed uniaxially. Under the assumption that only deviatoric stresses influence plasticity, one can argue that the plastic flow in the compressed disk is equivalent to the plastic flow under equi-biaxial tension (Barlat et al., 2003; Reyes et al., 2006). Thus, plastic strain measurements of the disk provide information that determines the gradient of the yield surface at the point of equi-biaxial tension through the equi-biaxial plastic strain ratio, which is defined as

$$R_{\mathrm{EqB}} = \frac{\varepsilon^{\mathrm{p}}_{yy}}{\varepsilon^{\mathrm{p}}_{xx}}.$$

Here, $\varepsilon^{\mathrm{p}}_{yy}$ and $\varepsilon^{\mathrm{p}}_{xx}$ are the plastic strains in the transversal and longitudinal material directions, respectively. The coin tests were conducted using the test set-up of Vysochinskiy (2014).

For the sheet material (6016 T4), crystallographic texture data were available in addition to the data from the uniaxial tensile and coin tests. From the texture data, a yield surface was calculated with the crystal plasticity finite element method (CP-FEM) using the method of Dumoulin et al. (2012). The parameters of the yield function were optimised to fit both the CP-FEM data and the uniaxial tensile test and coin test data (r-ratio, R-ratio and R_{EqB}), with a weight ratio of 1 to 100, respectively. For the extrusion material (6063 T6), texture data were not available and the parameters were solely optimised to the uniaxial tensile and coin test data. The resulting yield surface was instead correlated to previous work on the same alloy (Dumoulin et al., 2012), and satisfactory agreement was found.

The yield function parameters for both materials were found by minimising the sum of squares of error. The value of the exponent m was set to 8 in both cases, as this value has been shown to describe the behaviour of FCC materials (Barlat et al., 2005).

The hardening parameters were found through reverse engineering by simulating the uniaxial tensile test in the reference direction with the FE method using the explicit solver LS-DYNA® (version R7.1). The Levenberg-Marquardt algorithm was employed in the optimisation using the software LS-OPT® (version 5.0).

The resulting material model parameters are presented in Table 1. Graphical representations are presented in Figs. 8 and 9 for the two materials, respectively. The yield surfaces are represented as contours of the shear stress σ_{xy} projected onto the σ_x-σ_y-plane normalised to the yield stress σ_0 in Figs. 8a and 9a, while the experimental and computed r-values and R-values are presented in Figs. 8b, 8c, 9b and 9c. As shown, acceptable fits were achieved.

The sheet and extrusion both exhibited significant plastic anisotropy, whereas only slight anisotropy was observed for the flow stresses.

The FE model of the uniaxial tensile test in the reference direction is shown in Fig. 10a. The specimen was modelled with two symmetry planes: one in the thickness direction and one along the length of the specimen (dashed line). The model consisted of constant stress solid elements with reduced integration, with six elements through half the thickness in the central part. A tie constraint was applied between the coarse and fine mesh regions (red and blue parts in Fig. 10a), located such that they did not affect the results. In the physical tests, the specimens were simply supported with a pin through a hole in each end. The pins (yellow and green in Fig. 10a) were modelled as rigid bodies, and a node-to-surface algorithm was used for the contact between the pins and the specimen. A prescribed displacement along the longitudinal direction was enforced on one of the pins, whereas the other was fully clamped. Although the tests were conducted using a quasi-static strain rate, time scaling was applied in the simulations to reduce the computational time. Inertia effects were ensured to be negligible. The material model was implemented as a user material. The resulting engineering stress-strain curves are shown in Figs. 10b and 10c, which also include representative curves for the experiments. As shown in these figures, the results from the experiments were reproduced in the simulations.

3.3. Validation of material model

The material models were validated by challenging the yield surface outside the calibration domain using plane strain tension and in-plane single shear tests and corresponding simulations. Both the plane strain tension and the in-plane single shear specimens were cut out in the reference (rolling/extrusion) directions. The FE models are shown in Figs. 11a and 12a. These models were constructed in a manner similar to that of the uniaxial tension model (i.e., constant stress solid elements, reduced integration, symmetry planes where applicable, prescribed displacement, tie constraints, and time scaling), and the explicit solver LS-DYNA® (version R7.1) was again used. Six and ten elements were used through half the thickness, respectively. In the plane strain tension tests, mechanical grips were used for clamping, which was represented by modelling the outer parts as rigid bodies (green and yellow in Fig. 11a). The in-plane single shear test specimens were simply supported as in the uniaxial tensile tests with rigid body pins and a contact algorithm.

In the FE models of the material tests it was necessary to use solid elements, in order to accurately describe the specimen deformations at large strains (beyond diffuse necking). Shell elements are not sufficient to describe phenomena such as strain localization accurately. The obtained material model parameters were considered transferable to the large-scale simulations with shell elements in this work, as the plastic deformations of the shells were moderate, and no strain localization occurred in these simulations. For the same reason it was not necessary to include a fracture criterion.

The results of the validation simulations are shown in Figs. 11b, 11c, 12b and 12c in terms of force-displacement curves with representative curves for the experiments. As shown in these figures, the initial stiffness and the initiation

of yielding were correctly captured in all simulations. The work hardening in the plane strain tension tests was well captured for both materials. For the in-plane single shear test, the work hardening was well captured for the sheet, whereas it was somewhat over-estimated for the extrusion. This result is not believed to have a significant impact in the large-scale simulations in this work because the level of in-plane shear strains was limited.

4. Modelling of flow-drill screw connections

In this section, the investigated connection models are briefly presented. The element-based models are described first, followed by the constraint-based models and a summary highlighting the important differences between the models. The details of the models are presented in Appendix A. Readers are encouraged to read the appendix because the discussion in Section 5 involves details of the models. All the investigated models are available in the explicit FE solver LS-DYNA® version R7.1 (for *constrained interpolation spotweld* model 2 version R8.0 was used). The calibration/validation procedure is explained at the end of this section.

4.1. Element model 1

The first investigated model is *mat spotweld*, which was presented by Hallquist et al. (2007). For readability, this model is henceforth denoted as *element model 1*. This is a material model intended for beams and solid elements tied between two opposing shell surfaces (recall Fig. 1). It incorporates an isotropic elasto-plastic material model (J2 flow theory) with isotropic linear hardening coupled to different damage and failure models. This model was originally developed to model spot welds. The elasto-plastic behaviour is governed with four user parameters, i.e., Young's modulus E, Poisson's ratio ν, yield stress σ_y and plastic hardening modulus H. In addition, several other parameters linked to the different damage and failure models may be specified.

4.2. Element model 2

The second investigated element-based model is the tri-linear cohesive element model presented by Marzi et al. (2009) (henceforth denoted as *element model 2*). This model calculates the stresses on the mid-surface of the cohesive element as a function of the differences of the displacements of its upper and lower surfaces. This model is tri-linear in the sense that it incorporates linear elasticity, perfect plasticity and linear softening. Fig. 13a presents the tri-linear stress-separation curves for pure tensile and pure shear separation. Eight parameters define the tri-linear shape under pure tensile and pure shear loading, which also completely define the behaviour in mixed mode (Fig. 13b). This model is presented in detail in Appendix A.1.

4.3. Constraint model 1

This model (denoted as *constraint model 1*) was developed by Hanssen et al. (2010), and it was originally intended for self-piercing rivet connections. It includes a force-deformation model for uncoupled tensile and shear behaviour.

As deformation occurs, the model calculates the force and moment resultants, which are lumped to the nodes within a user-specified radius according to an interpolation function.

It it assumed that the rivet follows the motion of the master sheet, and the normal and tangential stretches δ_n and δ_t are calculated based on the relative displacement between the tail of the rivet and the slave sheet. A deformation history variable $\eta_{\max}$ is calculated using an interaction formula between δ_n and δ_t. This formula is scaled with a term that accounts for damage-dependent mode mixity dependency (Eq. (A.6)), where the mixed-mode response is governed by user parameters. The normal and tangential forces f_n and f_t are then directly calculated as functions of $\eta_{\max}$. The normal and tangential forces are applied to the nodes in the directions normal and tangential to the master sheet, respectively. Softening is obtained by damage coupling. The model is given in detail in Appendix A.2.

4.4. Constraint model 2

The second constraint-based model investigated is the first version of the model *constrained interpolation spotweld* (Hallquist et al., 2007) (henceforth denoted as *constraint model 2*). This model was originally intended for modelling spot-welded connections. Its numerical implementation is similar to that of *constraint model 1*. In *constraint model 2*, the connection is treated in a symmetrical manner. The stretches are defined from the relative displacement between the sheets, and the direction of the normal load is defined by the average vector between the unit normal of both sheets (see Eq. (A.8)). To capture sheet rotation, a third kinematical quantity, the relative rotation angle ω_b, is used.

The normal and tangential forces f_n and f_t and the moment m_b are calculated in an elasto-plastic manner, with a stiffness, a yield function, a flow rule, and a hardening rule. Softening is included by damage coupling. See Appendix A.3 for further details.

4.5. Constraint model 3

Bier and Sommer (2013) presented some modifications to *constrained interpolation spotweld* (the modified version is henceforth denoted as *constraint model 3*). The differences are manifested in the utilisation of ω_b and in the calculation of damage initiation and failure. See Appendix A.4 for details.

4.6. Summary of connection models

An overview of the models (except for *element model 1*) is given in Table 2 to highlight their similarities and differences. This table presents the definitions of kinematics, mode mixity angle, force computation and damage evolution.

A key difference between the models is the definition of the mode mixity angle. In *element model 2* and *constraint model 1*, the mode mixity angle is defined as a function of the stretches, whereas for *constraint model 2* and *constraint model 3*, it is defined from resultant forces. This difference was found to be important for the calibration and validation, as discussed in Section 5.

Another difference between the models is the calculation of stresses and forces. *Element model 2* is elasto-perfect plastic, but because the plasticity is ideal, it is not necessary to solve any non-linear equations linked to plasticity.

In *constraint model 1*, the forces are calculated directly from mathematical expressions. In *constraint model 2* and *constraint model 3*, however, an elasto-plastic formulation is used. To calculate the forces, a set of non-linear equations has to be solved.

Note that *element model 1* and *element model 2* have no flexibility for controlling the mixed-mode behaviour. In contrast, the constraint-based models do have parameters for controlling the mixed-mode behaviour. Due to this limitation, it was expected that better mixed-mode results would be obtained with the constraint-based models than with the element-based models.

4.7. Calibration/validation procedure

A robust validation procedure is important when modelling connections. The models should be calibrated to experiments with controlled macroscopic loading conditions. These tests should be easy to perform, and the number of tests needed should be limited to reduce the costs associated with the experiments, which is important from an industrial perspective.

Recall that a connection consists of the screw plus surrounding plate material (Fig. 2), and thus, the *macroscopic deformation* of a connection is *not* the same as the local deformations within the connection. Within the connection, the stress and deformation fields are complex and unknown, involving rotation of the screw and large plastic deformations and fracture of the plate materials. These deformations occur on a lower scale and can therefore not be captured by the macroscopic models. For this reason, the tests are discussed here on a macroscopic level.

Data from cross tests were used for calibration. The mechanical clamping of the plates in these tests constrained the deformation of the specimens such that the macroscopic deformation of the connections was approximately equal to the global displacement of the specimens. Thus, the macroscopic displacement path was simple and to some extent known. These tests were therefore well suited for calibration. Fig. 14a shows the calibration tests on a general fracture locus. The blue dots indicate the macroscopic connection displacement assumed in the tests.

The macroscopic models should subsequently be validated through another set of experiments. These experiments should challenge the connection under different loadings than the calibration tests and have varying degrees of complexity. A two-step validation strategy is proposed, as illustrated in Fig. 14b.

First, single lap joint and peeling tests were used for validation at the benchmark level. In these tests, the macroscopic deformation of the connections was non-proportional and less controlled than in the calibration tests. The single lap joint test was shear dominated, but due to less clamping close to the connection, the plates were less constrained and more free to rotate than in the cross shear test. This rotation introduced a varying tensile component of the macroscopic displacement of the connection. Similarly, in the peeling test, the macroscopic connection displacement was tensile dominated. During the test, the plates deformed, thereby introducing a shear component in the macroscopic connection displacement. Using these two tests for validation therefore provided useful information regarding the ability of the large-scale models to represent more challenging loadings. The benchmark tests are included in Fig. 14a, in which their approximate location on the fracture locus is indicated with green dots.

A second level of validation (component level) was obtained using T-component tests, which represent more complex and uncontrolled macroscopic loadings on the connections. Due to the unknown nature of the loading on the connections, it is possible that failure mechanisms different than those observed in the calibration tests occurred in the component tests. For instance, in axial crushing tests with the small screw connection, Sønstabø et al. (2015) observed failure due to shear fracture of the screw head and push-out of the screw due to contact between the tail and other parts of the specimen. These mechanisms were not observed in any other tests. Mechanisms that do not occur in calibration tests cannot be captured by macroscopic models. Additionally, the T-component specimens contained several connections next to each other (see Figs. 4a and 4b), which might induce interaction effects between them.

Tests on the product level (see Fig. 14b) are highly complex and expensive, and therefore, such test were not considered in this study.

Large-scale FE models of the calibration and validation tests were constructed. The connection model parameters were identified through reverse engineering of the cross tests. Force-displacement curves from the simulations were compared to the cross-head force and displacement in the experiments. The tension and shear parameters were optimised first, and then the mixed-mode parameters were optimised. Some parameters were taken directly from the experiments or manually tuned to fit the results. The Levenberg-Marquardt algorithm was used to optimise the remaining parameters, using the optimisation software LS-OPT® (version 5.0). After the model parameters were identified, they were validated with the benchmark and component simulations. The FE models used are presented in the following section.

4.8. FE models

The plates were modelled using Belytschko-Tsay shell elements with reduced integration with a mesh size of 2×2 mm. To limit the present study, the effect of mesh size in the plates was not investigated. Five integration points were used through the thickness. For contact between the different parts, a surface-to-surface algorithm with a penalty formulation was applied with a static friction coefficient of 0.2. The material models presented in Section 3 were applied to the sheet and extrusion materials. One plane of symmetry was utilised in the T-component simulation. The clamped parts were modelled as rigid bodies, and clamping was represented by constraining displacements. Loads were applied by enforcing displacements in the loading directions while constraining the other directions. The FE models are shown in Fig. 15a.

To obtain the hat- and U-shape of the sheets in the T-components and the bends of the sheets in the peeling specimens, the sheets were bent by pressing them into a die with a punch. The work hardening that occurred during the bending operation was investigated by simulating the bending process. The punch and die were modelled as rigid bodies, and the sheet was modelled using Belytschko-Tsay shell elements. To obtain a better description of the bend, a finer mesh size of 1×1 mm was used. The resulting fields of equivalent plastic strain and hardening variables for each through-thickness integration point were then mapped to the integration points in the bends of the peeling and T-component models. The process is illustrated in Fig. 15b, in which the fields of equivalent plastic strains are shown

as contour plots on the specimens. To account for the different mesh sizes in the mapping, the values inserted in the 2×2 mm elements were the average value of the corresponding two elements in the 1×1 mm mesh. To determine the effect of the work hardening, the large-scale simulations were run with and without the mapped fields. The results indicated that the work hardening had a limited effect on the simulation results.

5. Results and discussion

In the following, the results from the calibration and validation of the connection models are presented as force-displacement curves from simulations compared with experimental curves. The calibration is addressed first, followed by the validation. The discussion in Section 5.3 demonstrates the importance of having a proper validation procedure.

The element-based models are presented first, and then the constraint-based models are presented. The obtained parameters are summarised in Tables 3 and 4.

5.1. Calibration of element-based models

The results from the calibration of the element-based models are shown in Figs. 16 and 17, where the simulation and experimental curves are compared for both connections, respectively. As shown, the simulations and experiments match well in tension and shear (no damage/failure model was utilised in *element model 1*), but the force is severely over-predicted in mixed mode loading (Figs. 16b and 17b). As noted in Section 4.6, neither of the element-based models have flexibility for controlling the mixed mode behaviour; it is completely defined from the tension and shear parameters. It was therefore not possible to obtain more accurate results with these models, and they were determined to not be suitable for modelling flow-drill screw connections. Validation simulations were therefore not performed for the element-based models, and no damage/failure model was utilised in *element model 1*.

As stated in Table 3 the element cluster used with *element model 1* was comprised of 16 elements. This resulted in small elements, which decreased the time step and thus increased the computational time significantly, compared to the constraint-based models. This may be avoided by using fewer and larger elements in the cluster. With *element model 2* the time step was not affected. However, it was observed that the computational time was longer than for the constraint-based models by approximately a factor of 4.

5.2. Calibration of constraint-based models

The calibration results for the constraint-based models are shown for the two connections in Figs. 18 and 19, respectively. As shown in these figures, an acceptable fit was achieved in tension and shear for both connections for all three models. The initial stiffness, maximum force, ductility and overall shape of the curves were well captured. Some discrepancies are observed in the damage part in shear because all of the models predict linear softening in pure shear.

Under mixed mode loading, larger differences were observed. Consider the small screw connection (Fig. 18b). *Constraint model 1* over-estimated the initial stiffness and force level before maximum force. Softening was initiated

too early, but the model was flexible enough to correctly capture the displacement at failure. The initial stiffness and force level before maximum force were also over-estimated by *constraint model 2* and *constraint model 3*. For *constraint model 2*, good agreement was achieved for the damage part, whereas damage was initiated too early and failure occurred too late for *constraint model 3*. The level of maximum force was also relatively well captured by all of the models in mixed mode.

For the large screw connection under mixed mode loading (Fig. 19b), a relatively good fit was achieved by all of the models. Excellent agreement was obtained with *constraint model 1*. The force prior to maximum force was over-estimated by *constraint model 2* and *constraint model 3*.

No significant difference was observed between the computational times for the three constraint-based models. These simulations were, however, faster than the simulations with the element-based models. The presence of the connection models did not alter the critical time step.

5.2.1. Definition of mode mixity angle

At this point, it is worthwhile to discuss some points associated with the mode mixity angle definition in *constraint model 2* and *constraint model 3*. Recall that for these models, the mode mixity angle θ is defined as a function of the ratio of forces (see Eqs. A.13 and A.17). This way of defining θ resulted in some challenges associated with calibration. When simulating the cross tension and cross shear tests, θ was, as expected, close to 90° and 0°, respectively. During the cross mixed simulations, however, θ varied between 5° and 20° due to varying forces for both connections. This had different implications on the calibration of the damage part for *constraint model 2* and *constraint model 3*, as explained in the following.

Recall that for *constraint model 2*, the relative plastic motions at damage initiation and failure, $\bar{u}_0^{\text{pl}}(\theta)$ and $\bar{u}_f^{\text{pl}}(\theta)$, must be tabulated by the user. Each of the three calibration tests provides one point in each tabulated function. Values were obtained for $\theta = 90°$ and $\theta = 0°$ by reverse engineering the cross tension and cross shear tests, respectively. However, because θ varied between 5° and 20° during the cross mixed simulations, a compromise had to be made, and data points associated with the cross mixed tests were tabulated for $\theta = 10°$. Furthermore, to capture the damage behaviours observed in the tests, the relative plastic motions at damage initiation and failure in shear ($\theta = 0°$) had to be different from mixed mode ($\theta = 10°$). Consequently, the relative plastic motions at damage initiation and failure were very sensitive to variations in θ for low values of θ (close to pure shear). This is illustrated in Fig. 20a, which shows two possible interaction curves for relative plastic motions at damage initiation and failure. The axes are labelled with both $\bar{u}_0^{\text{pl}}$ and $\bar{u}_f^{\text{pl}}$ to indicate that this challenge occurs for both the damage initiation and failure curves. In the dashed curve, the values in shear are larger than the values in mixed mode, and in the solid curve, the values in mixed mode are larger. For both cases, a small variation in θ close to $\theta = 0°$ leads to a large variation in the values of $\bar{u}_0^{\text{pl}}(\theta)$ and $\bar{u}_f^{\text{pl}}(\theta)$. Consequently, if the mode mixity angle in a simulation varies from 0° to 10°, the response quickly changes from that of cross shear to that of cross mixed. This was indeed the case for the single lap joint simulations, as will be discussed in Section 5.3.

For *constraint model 3*, damage initiation and failure displacements are given by the interaction formulas in Eqs. A.15 and A.16. These formulas include parameters for relative displacement at damage initiation and failure in pure tension and pure shear, which were found by reverse engineering the cross tension and cross shear tests, respectively. The interaction curves are super-ellipses, whose shapes are determined by the exponents β_2 and β_3, which were calibrated by reverse engineering the cross mixed tests. However, because the mode mixity angle in the cross mixed simulation was so close to pure shear, different values of the exponents had little impact on the response in this simulation, as illustrated in Fig. 20b. As shown, the values of $\bar{u}_0^{\mathrm{pl}}$ and $\bar{u}_f^{\mathrm{pl}}$ in the cross mixed simulation were more or less locked to the value in pure shear. The mixed mode flexibility of this model could therefore not be fully utilised. This is believed to be the reason why softening was poorly represented by this model in the cross mixed simulations (Figs. 18b and 19b).

A remedy to these challenges could be to introduce additional calibration tests with mode mixities further away from pure shear. However, from an industry perspective, it is desirable to keep the number of tests as low as possible to minimise the costs. Additionally, several validation tests are needed for robustness of the validation procedure. Therefore, the number of calibration tests was limited to three in this work. As an example, Bier and Sommer (2013) used five different tests for calibration and one for validation.

In *constraint model 1*, the mode mixity angle is defined as a function of the stretches (Eq. (A.7)). With this definition, the mode mixity angles in the simulations were close to the global loading angle in the tests (90°, 45° and 0° for cross tension, mixed and shear, respectively). Thus, the challenges associated with the calibration of *constraint model 2* and *constraint model 3* did not arise for this model. Higher flexibility was obtained in the cross mixed simulations, and the model was easier to calibrate.

5.2.2. Influence of relative rotation angle ω_b

To account for the relative rotation between the sheets, *constraint model 2* and *constraint model 3* utilise the relative rotation angle ω_b (Eq. (A.9)). The influence of the relative rotation is adjusted by user parameters (see Eqs. (A.11), (A.14), (A.15) and (A.16)). However, the influence of the relative rotation was set to zero in this work. The reason for this choice is two-fold.

First, to calibrate the influence parameters, experimental tests with significant relative sheet rotations are needed. Thus, additional calibration tests are required, which is undesirable from a cost perspective. Bier and Sommer (2013) proposed calibrating the influence parameters using peeling tests. However, this approach is also undesirable because it will remove a validation test and thus weaken the validation strategy.

Second, the only simulation that would be affected by including the influence of relative rotation in this work is the peeling simulation. In all other simulations, the relative rotation between the sheets is negligible. As will be shown in Section 5.3, the results of the peeling simulations are already satisfactory without the influence of relative rotation.

5.3. Validation of constraint-based models

For the calibration simulations, the choice of constraint-based model had no significant influence on the computational time of the validation simulations. The numerical and experimental results from the validation tests (single lap joint, peeling and T-component) for the two connections are presented in Figs. 21 and 22, respectively.

For the single lap joint tests (Figs. 21a and 22a), *constraint model 1* provided good predictions for both connections. The force level and the softening were well captured. For the small screw connection, the initial stiffness was somewhat under-estimated by all models. The force level and softening were poorly described by *constraint model 2* and *constraint model 3* for both connections. This result may be explained by the challenges associated with the mode mixity definition (see Section 5.2.1). Recall that the mode mixity angle in the cross mixed simulations ranged between 5° and 20° and that the models were therefore calibrated to the cross mixed results for this angle. However, in the single lap joint simulations the mode mixity angle also varied between 5° and 20°. Consequently, the damage evolution of *constraint model 2* and *constraint model 3* could not discern between cross mixed and single lap joint simulations, even though the physical behaviours in the tests were different. This becomes clear when comparing Fig. 21a and 22a with Figs. 18b and 19b. As shown in these figures, the responses are similar. This clearly demonstrates the challenge with the mode mixity angle defined by resultant forces.

Acceptable fits were obtained in the peeling simulations (Figs. 21b and 22b). For the small screw connection, the force levels before maximum force were in good agreement with the experiments. The maximum force was over-predicted by all models, which was caused by over-predicting the ductility. For the large screw connection, the maximum force was under-predicted by all models. As explained in Section 2, rotation of the screw caused the screw tail to come into contact with the extruded plate, thereby causing the higher force slope occurring at approximately 2 kN (see Fig. 22b). This physical effect cannot be captured by the investigated models; thus, the under-prediction of the maximum force was expected. The displacement at failure was over-predicted by *constraint model 1*, whereas *constraint model 2* and *constraint model 3* were in good agreement with the experiments for this part.

Generally good predictions of the maximum force level were achieved for all models in the T-component simulations. For the small screw connection, *constraint model 2* over-estimated the maximum force, and all models over-estimated the ductility (Fig. 21c). A possible explanation for the latter is the abrupt fracture behaviour that was observed in the T-component tests but not in the cross shear tests. For the large screw connection (Fig. 22c), good agreement between the simulations and experiments was obtained. *Constraint model 2* under-estimated the maximum force level by a small fraction, and *constraint model 1* slightly over-estimated the ductility.

By comparing the T-component simulations (Figs. 21c and 22c) with the cross mixed (Figs. 18b and 19b) and the single lap joint simulations (Figs. 21a and 22a), similarities are observed in the shapes of the curves, particularly in the softening parts. This result may indicate that the T-component simulations were also affected by the problem of the mode mixity definition. This is supported by the fact that the mode mixity angle for the connections varied between 0° and 25° in the simulations.

In summary, of the five connection models investigated, *constraint model 1* appears to be the most suited for

modelling flow-drill screw connections. This model appears to be the most robust, providing the most accurate reproduction of the calibration and validation tests for both connections. Furthermore, this model was the easiest to calibrate. The challenges discussed in this section demonstrate that it is indeed important to have a proper validation strategy in which the models are challenged in different ways than in the calibration tests.

5.4. Static vs. dynamic problems

As all tests in this work were quasi-static, the discussed modelling techniques have been assessed for static problems. Currently there is a lack of published experimental data from dynamic testing of FDS connections. Whether or not the modelling techniques presented here are applicable to dynamic problems is therefore an open question. However, Porcaro et al. (2008) performed dynamic tests of a self-piercing rivet connection under tension and shear, and observed no significant rate-effect on the resulting force-displacement curves or failure modes. Furthermore, Sønstabø et al. (2015) showed that self-piercing rivet connections and FDS connections behave in a similar way. Considering the observed similarities, and the fact that the aluminium alloys used in this work exhibit insignificant strain-rate dependence, it is believed that the obtained model parameters are usable for the dynamic regime as well as the static.

6. Conclusions

Five different macroscopic models were evaluated for modelling flow-drill screw connections in thin-walled aluminium structures. These models were calibrated to cross tests and validated first with single lap joint and peeling tests and then with T-component tests. The following main conclusions may be drawn from the present investigation:

- A two-step validation strategy for modelling flow-drill screw connections was presented and used. The validation consisted of benchmark and peeling tests. The validation results demonstrated the need to have a proper validation strategy.
- Of the investigated models, *constraint model 1* was the most suitable for describing flow-drill screw connections. This model provided the best results and was the easiest to calibrate.
- The two element-based models were not sufficiently flexible to represent the cross mixed tests and were thus not validated.
- The definition of the mode mixity angle as a function of forces in *constraint model 2* and *constraint model 3* was a challenge for modelling flow-drill screw connections.

Acknowledgements

Acknowledgements are made to Honda R&D Americas, Inc., and Centre for Advanced Structural Analysis (CASA), Department of Structural Engineering at Norwegian University of Science and Technology (NTNU) for financial support.

References

F Barlat, JC Brem, JW Yoon, K Chung, RE Dick, DJ Lege, F Pourboghrat, S-H Choi, and E Chu. Plane stress yield function for aluminum alloy sheets—part 1: theory. *International Journal of Plasticity*, 19(9):1297–1319, 2003.

F. Barlat, H. Aretz, J.W. Yoon, M.E. Karabin, J.C. Brem, and R.E. Dick. Linear transfomation-based anisotropic yield functions. *International Journal of Plasticity*, 21(5):1009 – 1039, 2005. ISSN 0749-6419. doi: http://dx.doi.org/10.1016/j.ijplas.2004.06.004. URL `http://www.sciencedirect.com/science/article/pii/S0749641904001160`.

M Bier and S Sommer. Simplified modeling of self-piercing riveted joints for crash simulations with a modified version of constrained_interpolation_spotweld. In *9th European LS-DYNA Conference, Manchester*, 2013.

M Bier, C Liebold, A Haufe, and H Klamser. Evaluation of a rate-dependent, elasto-plastic cohesive zone mixed-mode constitutive model for spot weld modeling. In *LS-DYNA Forum, Bamberg*, 2010.

Thomas Carlberger and Ulf Stigh. Dynamic testing and simulation of hybrid joined bi-material beam. *Thin-walled structures*, 48(8):609–619, 2010.

S Dumoulin, O Engler, OS Hopperstad, and OG Lademo. Description of plastic anisotropy in aa6063-t6 using the crystal plasticity finite element method. *Modelling and Simulation in Materials Science and Engineering*, 20(5):055008, 2012.

John O Hallquist et al. Ls-dyna keyword user's manual. *Livermore Software Technology Corporation*, 970, 2007.

AG Hanssen, L Olovsson, R Porcaro, and M Langseth. A large-scale finite element point-connector model for self-piercing rivet connections. *European Journal of Mechanics-A/Solids*, 29(4):484–495, 2010.

N-H Hoang, A-G Hanssen, M Langseth, and R Porcaro. Structural behaviour of aluminium self-piercing riveted joints: An experimental and numerical investigation. *International Journal of Solids and Structures*, 49(23):3211–3223, 2012.

O.-G. Lademo, O.S. Hopperstad, and M. Langseth. An evaluation of yield criteria and flow rules for aluminium alloys. *International Journal of Plasticity*, 15(2):191 – 208, 1999. ISSN 0749-6419. doi: http://dx.doi.org/10.1016/S0749-6419(98)00064-3. URL `http://www.sciencedirect.com/science/article/pii/S0749641998000643`.

Skye Malcolm and Emily Nutwell. Spotweld failure prediction using solid element assemblies. In *6th European LS-Dyna users' conference. Gothenburg, Sweden*, 2007.

Stephan Marzi, Olaf Hesebeck, Markus Brede, and Felix Kleiner. A rate-dependent, elasto-plastic cohesive zone mixed-mode model for crash analysis of adhesively bonded joints. In *7th European LS-DYNA conference*, 2009.

R Porcaro, M Langseth, AG Hanssen, Heyuan Zhao, S Weyer, and H Hooputra. Crashworthiness of self-piercing riveted connections. *International Journal of Impact Engineering*, 35(11):1251–1266, 2008.

A. Reyes, O.S. Hopperstad, O.-G. Lademo, and M. Langseth. Modeling of textured aluminum alloys used in a bumper system: Material tests and characterization. *Computational Materials Science*, 37(3):246 – 268, 2006. ISSN 0927-0256. doi: http://dx.doi.org/10.1016/j.commatsci.2005.07.001. URL `http://www.sciencedirect.com/science/article/pii/S0927025605002582`.

F Seeger, M Feucht, Th Frank, B Keding, and A Haufe. An investigation on spot weld modelling for crash simulation with ls-dyna. In *4th LS-DYNA User Forum, Bamberg*, 2005.

Johan Kolstø Sønstabø, Petter Henrik Holmstrøm, David Morin, and Magnus Langseth. Macroscopic strength and failure properties of flow-drill screw connections. *Journal of Materials Processing Technology*, 222(0):1 – 12, 2015. ISSN 0924-0136. doi: http://dx.doi.org/10.1016/j.jmatprotec.2015.02.031. URL `http://www.sciencedirect.com/science/article/pii/S0924013615000813`.

Silke Sommer and Johannes Maier. Failure modeling of a self piercing riveted joint using ls-dyna. In *8th LS-DYNA European Conference, May*, pages 23–24, 2008.

Dmitry Vysochinskiy. *Formability of aluminium alloy subjected to prestrain by rolling*. PhD thesis, Norwegian University of Science and Technology, 2014.

Minoru Yamashita, Hiromasa Kenmotsu, and Toshio Hattori. Dynamic crush behavior of adhesive-bonded aluminum tubular structure—experiment and numerical simulation. *Thin-Walled Structures*, 69:45 – 53, 2013. ISSN 0263-8231. doi: http://dx.doi.org/10.1016/j.tws.2013.04.005. URL `http://www.sciencedirect.com/science/article/pii/S0263823113000839`.

A. Details of macroscopic models

A.1. Element model 2

This is the cohesive element model presented by Marzi et al. (2009).

The tri-linear stress-separation curves for pure normal and pure shear loadings are presented in Fig. 13a. The shapes of the curves are defined by user parameters as follows. The total area (energy) under the curves is defined by G_n and G_t. Henceforth, the subscripts n and t denote pure normal and pure tangential loadings, respectively. The elastic stiffnesses E_n and E_t are calculated by

$$E_n = \frac{E}{t}$$
$$E_t = \frac{G}{t},$$

where E and G are the Young's and shear moduli provided by the user and t is the thickness of the cohesive element. The yield stresses N and T are defined by the user. The last parameters needed for defining the shape of the stress-separation curves are the areas under the plastic parts, given as fractions f_{Gn} and f_{Gt} of the total areas. That is,

$$0 \leq f_{Gn} = \frac{G_n^p}{G_n} < 1 - \frac{N^2}{2G_nE_n}$$
$$0 \leq f_{Gt} = \frac{G_t^p}{G_t} < 1 - \frac{T^2}{2G_tE_t}.$$

The plastic areas G_n^p and G_t^p cannot include the elastic areas (hence the right inequalities).

The yield initiation displacements δ_{n1} and δ_{t1} may now be calculated as

$$\delta_{n1} = \frac{N}{E_n}$$
$$\delta_{t1} = \frac{T}{E_t}.$$

The yield initiation displacement in mixed mode, δ_{m1}, is calculated using a quadratic interaction formula as follows,

$$\delta_{m1} = \delta_{n1}\delta_{t1}\sqrt{\frac{1+\beta^2}{\delta_{t1}^2 + (\beta\delta_{n1})^2}},$$

where

$$\beta = \frac{\Delta_t}{\Delta_n}.$$

Note that there is a mistake in the definition of β in the references (Marzi et al., 2009; Hallquist et al., 2007). The above definition is correct.

Similarly, the mixed-mode damage initiation displacement is defined as

$$\delta_{m2} = \delta_{n2}\delta_{t2}\sqrt{\frac{1+\beta^2}{\delta_{t2}^2 + (\beta\delta_{n2})^2}},$$

where

$$\delta_{n2} = \delta_{n1} + \frac{f_{Gn} G_n}{N}$$
$$\delta_{t2} = \delta_{t1} + \frac{f_{Gt} G_t}{T}.$$

The failure displacement in mixed mode, δ_{mf}, is defined as (see the paper of Marzi et al. (2009) for explanation)

$$\delta_{mf} = \frac{\delta_{m1}\left(\delta_{m1} - \delta_{m2}\right) E_n G_t \cos^2\theta + G_n \left(2G_t + \delta_{m1}(\delta_{m1} - \delta_{m2}) E_t \sin^2\theta\right)}{\delta_{m1}\left(E_n G_t \cos^2\theta + E_t G_n \sin^2\theta\right)},$$

where

$$\theta = \arccos \frac{\langle u_n \rangle}{\Delta_m}.$$

With this, the shape of the mixed-mode stress-separation curve is determined (see Fig. 13b), and the stresses may be calculated, as shown in the following. Let u_n, u_{t1} and u_{t2} denote the element's relative displacements in the normal and in both tangential directions of the element coordinate system in the mid-plane. Then, the two separations Δ_n in the normal direction and Δ_t in the shear direction are defined as follows,

$$\Delta_n = \max(u_n, 0)$$
$$\Delta_t = \sqrt{u_{t1}^2 + u_{t2}^2}.$$

The total separation (mixed mode) Δ_m is further defined as

$$\Delta_m = \sqrt{\Delta_n^2 + \Delta_t^2}.$$

The plastic separations in each element direction, u_n^p, u_{t1}^p and u_{t2}^p, may now be calculated. In the normal direction, the plastic separation is given by

$$u_n^p = \max\left(u_{n,\Delta t-1}^p, u_n - \delta_{m1}\cos\theta, 0\right),$$

where the subscript $\Delta t - 1$ denotes the variable at the previous time step. Thus, if plasticity occurs, the plastic normal separation is equal to the total normal separation minus the elastic part. If loading is purely elastic, then the plastic normal separation remains zero or equal to the value at the previous time step.

For the shear direction, a shear yield separation δ_{ty} is defined as

$$\delta_{ty} = \sqrt{\left(u_{t1} - u_{t1,\Delta t-1}^p\right)^2 + \left(u_{t2} - u_{t2,\Delta t-1}^p\right)^2}.$$

If $\delta_{ty} > \delta_{m1}\sin\theta$, then plasticity occurs, and u_{t1}^p and u_{t2}^p are updated according to

$$u_{t1}^p = u_{t1,\Delta t-1}^p + \left(u_{t1} - u_{t1,\Delta t-1}\right)$$
$$u_{t2}^p = u_{t2,\Delta t-1}^p + \left(u_{t2} - u_{t2,\Delta t-1}\right).$$

If $\Delta m > \delta_{m2}$, then a damage variable d increases linearly,

$$d = \max\left(\frac{\Delta_m - \delta_{m2}}{\delta_{mf} - \delta_{m2}}, d_{\Delta t-1}, 0\right).$$

When d reaches unity, damage is complete and the integration point fails.

The stresses in the element coordinate system may now be calculated. In the normal direction, damage is only considered under tensile loading. That is, if $u_n - u_n^p < 0$,

$$\sigma_n = E_n\left(u_n - u_n^p\right);$$

otherwise,

$$\sigma_n = E_n\left(1 - d\right)\left(u_n - u_n^p\right).$$

The shear stresses are

$$\sigma_{t1} = E_t\left(1 - d\right)\left(u_{t1} - u_{t1}^p\right)$$
$$\sigma_{t2} = E_t\left(1 - d\right)\left(u_{t2} - u_{t2}^p\right).$$

Rate dependency may be included, but it was not considered in this work.

A.2. Constraint model 1

This model was originally developed by Hanssen et al. (2010) for self-piercing rivet connections.

The kinematics of the model are shown in Fig. 23a. All considerations of the model are performed in the so-called plane of maximum opening, which is defined by the normal vector

$$\mathbf{n}_0 = \mathbf{n}_s \times \mathbf{n}_m, \tag{A.1}$$

where $\mathbf{n}_s$ and $\mathbf{n}_m$ are the unit normal vectors of the slave and master sheets, respectively. The tangential unit vector of the rivet is defined by

$$\mathbf{n}_t = \mathbf{n}_0 \times \mathbf{n}_m. \tag{A.2}$$

It is assumed that the rivet is following the motion of the master sheet (see Fig. 23a). The local deformation of the rivet is given by the normal stretch vector $\mathbf{\Delta}_n$ and the tangential stretch vector $\mathbf{\Delta}_t$. Total stretch $\mathbf{\Delta} = \mathbf{\Delta}_n + \mathbf{\Delta}_t$ is defined as the vector between the slave end and its original location on the deformed slave sheet (see Fig. 23a), from which the scalar normal and tangential stretches may be computed as

$$\Delta_n = |\mathbf{\Delta} \cdot \mathbf{n}_m|$$
$$\Delta_t = |\mathbf{\Delta} \cdot \mathbf{n}_t|. \tag{A.3}$$

The model calculates the normal and tangential forces, f_n and f_t, based on the deformation and deformation history of the rivet, as explained in the following.

The normal and tangential forces are calculated according to

$$f_n = \frac{f_n^{\max}\Delta_n}{\eta_{\max}\Delta_n^{\text{fail}}}\hat{f}_n\left(\eta_{\max}\right) \tag{A.4}$$

$$f_t = \frac{f_t^{\max}\Delta_t}{\eta_{\max}\Delta_t^{\text{fail}}}\hat{f}_t\left(\eta_{\max}\right), \tag{A.5}$$

where

$$\hat{f}_n\left(\eta_{\max}\right) = \begin{cases} 1 - \left(\dfrac{\xi_n - \eta_{\max}}{\xi_n}\right)^8 & \eta_{\max} \le \xi_n \\ 1 - \dfrac{\eta_{\max} - \xi_n}{1 - \xi_n} & \eta_{\max} > \xi_n \end{cases}$$

$$\hat{f}_t\left(\eta_{\max}\right) = \begin{cases} 1 - \left(\dfrac{\xi_t - \eta_{\max}}{\xi_t}\right)^8 & \eta_{\max} \le \xi_t \\ 1 - \dfrac{\eta_{\max} - \xi_t}{1 - \xi_t} & \eta_{\max} > \xi_t \end{cases}.$$

The parameters $f_n^{\max}$, $f_t^{\max}$, Δ_n^{fail}, Δ_t^{fail}, ξ_n and ξ_t are determined by the user, and $\eta_{\max}$ is defined as

$$\eta_{\max} = \max\left(\eta(t)\right).$$

The effective displacement measure $\eta(t)$ is defined by a scaled interaction formula as follows,

$$\eta(\theta, \eta_{\max}, t) = \left[\xi(\theta) + \frac{1 - \xi(\theta)}{\alpha\left(\eta_{\max}\right)}\right]\sqrt{\left(\frac{\Delta_n(t)}{\Delta_n^{\text{fail}}}\right)^2 + \left(\frac{\Delta_t(t)}{\Delta_t^{\text{fail}}}\right)^2}, \tag{A.6}$$

where θ is the mode mixity angle defined by the kinematical motion (stretches) as

$$\theta = \arctan\left(\frac{\Delta_n}{\Delta_t}\right). \tag{A.7}$$

The scaling factor in Eq. (A.6) contains the parameter $\xi(\theta)$, which scales the effective displacement as a function of the mode mixity angle according to the polynomial

$$\xi(\theta) = 1 - \frac{27}{4}\left(\frac{2\theta}{\pi}\right)^2 + \frac{27}{4}\left(\frac{2\theta}{\pi}\right)^3.$$

The parameter $\alpha\left(\eta_{\max}\right)$ is included in Eq. (A.6) to allow the directional scaling of the effective displacement to be damage dependent, and it is defined as follows,

$$\alpha\left(\eta_{\max}\right) = \begin{cases} \dfrac{\xi_t - \eta_{\max}}{\xi_t}\alpha_1 + \dfrac{\eta_{\max}}{\xi_t}\alpha_2 & \eta_{\max} < \xi_t \\ \dfrac{1 - \eta_{\max}}{1 - \xi_t}\alpha_2 + \dfrac{\eta_{\max} - \xi_t}{1 - \xi_t}\alpha_3 & \eta_{\max} \ge \xi_t \end{cases},$$

where α_1, α_2 and α_3 are user parameters.

After the forces have been determined using Eqs. (A.4) and (A.5), the moments at the master and slave ends, M_m and M_s, respectively, are calculated using the relations

$$M_m = \begin{cases} \dfrac{h_m + h_s}{4} f_t & \eta_{\max} < \xi_t \\ \dfrac{h_m + h_s}{4} \left(1 + \dfrac{\eta_{\max} - \xi_t}{1 - \xi_t}\right) f_t & \eta_{\max} \geq \xi_t \end{cases}$$

$$M_s = \begin{cases} \dfrac{h_m + h_s}{4} f_t & \eta_{\max} < \xi_t \\ \dfrac{h_m + h_s}{4} \left(1 - \dfrac{\eta_{\max} - \xi_t}{1 - \xi_t}\right) f_t & \eta_{\max} \geq \xi_t \end{cases},$$

where h_m and h_s are the thicknesses of the master and slave sheet, respectively. Moment balance is thus satisfied.

To summarise, six parameters are required to define the behaviour in pure tension ($f_n^{\max}$, Δ_n^{fail}, and ξ_n) and pure shear ($f_t^{\max}$, Δ_t^{fail}, and ξ_t). Flexibility in mixed mode is obtained with the three parameters α_1, α_2 and α_3. In addition, the radius of influence r, within which the forces and moments are lumped to the nodes on each shell surface, must be specified (see Fig. 1e).

A.3. Constraint model 2

This is the model *constrained interpolation spotweld* available in LS-DYNA® (Hallquist et al., 2007).

The kinematics of this model are different than *constraint model 1*, as shown in Fig. 23b. As for *constraint model 1*, all considerations are performed in the plane of maximum opening (Eq. (A.1)). The connection is, however, treated symmetrically, which means that the rivet is not following the master sheet. Rather, a unit vector defines the direction of normal loads as the average of the unit normals of the sheets (see Fig. 23b),

$$\mathbf{n}_n = \frac{\mathbf{n}_m + \mathbf{n}_s}{|\mathbf{n}_m + \mathbf{n}_s|}. \tag{A.8}$$

The corresponding tangential direction is given by

$$\mathbf{n}_t = \mathbf{n}_0 \times \mathbf{n}_n.$$

The total stretch $\mathbf{\Delta}$ is defined here as the relative displacement between the two sheets (see Fig. 23b),

$$\mathbf{\Delta} = \mathbf{u}_2 - \mathbf{u}_1,$$

where $\mathbf{u}_1$ and $\mathbf{u}_2$ are the displacement vectors of the two sheets. The scalar normal and tangential stretches may then be calculated as

$$\Delta_n = |\mathbf{\Delta} \cdot \mathbf{n}_n|$$

$$\Delta_t = |\mathbf{\Delta} \cdot \mathbf{n}_t|.$$

To capture the relative rotation between the sheets, a third kinematical quantity ω_b is defined as the angle between the shell normals in the plane of maximum opening (see Fig. 23b),

$$\omega_b = \arccos \frac{\mathbf{n}_s \cdot \mathbf{n}_m}{|\mathbf{n}_s|\,|\mathbf{n}_m|}. \tag{A.9}$$

The corresponding forces f_n and f_t and the moment m_b are calculated in an elastic-plastic manner, with a stiffness E, a yield function, a flow rule and a hardening rule. Linear mode mixity-dependent damage is incorporated. An effective elastic force vector is defined as

$$\tilde{\mathbf{f}} = [f_n, f_t, m_b] = E\,[\Delta_n, \Delta_t, \omega_b] = E\mathbf{u}.$$

The yield function is defined as

$$\phi\left(\tilde{\mathbf{f}}, \bar{u}^{\mathrm{pl}}\right) = P\left(\tilde{\mathbf{f}}\right) - F^0\left(\bar{u}^{\mathrm{pl}}\right) \leq 0, \tag{A.10}$$

where the potential $P\left(\tilde{\mathbf{f}}\right)$ is defined as

$$P\left(\tilde{\mathbf{f}}\right) = \left[\left(\frac{f_n + \alpha_1 m_b}{R_n}\right)^{\beta_1} + \left(\frac{f_t}{R_t}\right)^{\beta_1}\right]^{\frac{1}{\beta_1}}. \tag{A.11}$$

The parameters R_n, R_t, β_1 and α_1 are determined by the user. Furthermore, associated flow is assumed such that the rate of plastic relative motion $\dot{\mathbf{u}}^{\mathrm{pl}}$ is defined as

$$\dot{\mathbf{u}}^{\mathrm{pl}} = \dot{\bar{u}}^{\mathrm{pl}} \frac{\partial \phi}{\partial \tilde{\mathbf{f}}}.$$

Here, $\dot{\bar{u}}^{\mathrm{pl}}$ is the plastic multiplier, which must be non-negative to ensure non-negative plastic dissipation. The equivalent plastic relative motion $\bar{u}_{\mathrm{pl}}$ is then defined as

$$\bar{u}^{\mathrm{pl}} = \int_0^t \dot{\bar{u}}^{\mathrm{pl}} \mathrm{d}t,$$

and is thus positive and always increasing with plasticity (it serves the same function as the equivalent plastic strain in regular plasticity theory). Note that $\bar{u}^{\mathrm{pl}}$ has units of force times length.

Analogous to regular plasticity theory, loading/unloading conditions may be summarised as

$$\phi \leq 0$$
$$\dot{\bar{u}}^{\mathrm{pl}} \geq 0$$
$$\dot{\bar{u}}^{\mathrm{pl}} \phi = 0,$$

and the consistency condition states that

$$\dot{\bar{u}}^{\mathrm{pl}} \dot{\phi} = 0.$$

The term $F^0\left(\bar{u}^{\mathrm{pl}}\right)$ in Eq. (A.10) is an isotropic hardening function defined by the user, and in this work, it was defined as a Voce-like function as follows,

$$F^0\left(\bar{u}^{\mathrm{pl}}\right) = R_0 + Q_1\left(1 - \exp\left(-\frac{\theta_1}{Q_1}\bar{u}^{\mathrm{pl}}\right)\right).$$

where R_0, Q_1 and θ_1 are user parameters.

The nominal force vector $\mathbf{f}$ is scaled by a damage variable as follows,

$$\mathbf{f} = (1 - d)\,\tilde{\mathbf{f}},$$

where

$$d = \begin{cases} 0 & \bar{u}^{\mathrm{pl}} < \bar{u}_0^{\mathrm{pl}}(\theta) \\ \dfrac{\bar{u}^{\mathrm{pl}} - \bar{u}_0^{\mathrm{pl}}(\theta)}{\bar{u}_f^{\mathrm{pl}}(\theta)} & \bar{u}^{\mathrm{pl}} \geq \bar{u}_0^{\mathrm{pl}}(\theta) \end{cases}. \tag{A.12}$$

Here, $\bar{u}_0^{\mathrm{pl}}(\theta)$ is the plastic relative motion at damage initiation and $\bar{u}_0^{\mathrm{pl}}(\theta) + \bar{u}_f^{\mathrm{pl}}(\theta)$ is the plastic relative motion at failure. They are defined by the user as tabulated functions of the mode mixity angle θ, which is defined in terms of resultant forces as follows,

$$\theta = \arctan\left(\frac{f_n + \alpha_1 m_b}{f_t}\right). \tag{A.13}$$

Thus, the parameters that must be determined by the user are E, R_n, R_t, β_1 and α_1; the functions $\bar{u}_0^{\mathrm{pl}}(\theta)$ and $\bar{u}_f^{\mathrm{pl}}(\theta)$; the radius of influence r; and the hardening parameters R_0, Q_1 and θ_1. In this work, α_1 was set to zero.

A.4. Constraint model 3

Bier and Sommer (2013) presented some modifications to constraint model 2. The differences are addressed in the following.

First, the relative rotation angle ω_b is omitted from the vector of relative motion $\mathbf{u}$,

$$\mathbf{u} = [\Delta_n, \Delta_t],$$

and the corresponding force vector is given by

$$\mathbf{f} = [f_n, f_t].$$

The relative rotation angle is instead included in the potential in Eq. (A.10) as follows,

$$P\left(\tilde{\mathbf{f}}\right) = \left[\left(\frac{f_n}{R_n\left(1 - \alpha_1 \omega_b\right)}\right)^{\beta_1} + \left(\frac{f_t}{R_t}\right)^{\beta_1}\right]^{\frac{1}{\beta_1}}. \tag{A.14}$$

Second, the calculation of damage initiation and failure is performed differently. The damage variable is defined by

Eq. (A.12), but $\bar{u}_0^{\mathrm{pl}}(\theta)$ and $\bar{u}_f^{\mathrm{pl}}(\theta)$ are determined by solving the following system of six equations

$$\left[\left(\frac{\bar{u}_0^{\mathrm{pl},n}}{\bar{u}_{0,\mathrm{ref}}^{\mathrm{pl},n}\left(1-\alpha_2\omega_b\right)}\right)^{\beta_2}+\left(\frac{\bar{u}_0^{\mathrm{pl},t}}{\bar{u}_{0,\mathrm{ref}}^{\mathrm{pl},t}}\right)^{\beta_2}\right]^{\frac{1}{\beta_2}}=1 \tag{A.15}$$

$$\bar{u}_0^{\mathrm{pl},n}=\sin\left(\theta\right)\bar{u}_0^{\mathrm{pl}}$$

$$\bar{u}_0^{\mathrm{pl},t}=\cos\left(\theta\right)\bar{u}_0^{\mathrm{pl}}$$

$$\left[\left(\frac{\bar{u}_f^{\mathrm{pl},n}}{\bar{u}_{f,\mathrm{ref}}^{\mathrm{pl},n}\left(1-\alpha_3\omega_b\right)}\right)^{\beta_3}+\left(\frac{\bar{u}_f^{\mathrm{pl},t}}{\bar{u}_{f,\mathrm{ref}}^{\mathrm{pl},t}}\right)^{\beta_3}\right]^{\frac{1}{\beta_3}}=1 \tag{A.16}$$

$$\bar{u}_f^{\mathrm{pl},n}=\sin\left(\theta\right)\bar{u}_f^{\mathrm{pl}}$$

$$\bar{u}_f^{\mathrm{pl},t}=\cos\left(\theta\right)\bar{u}_f^{\mathrm{pl}}.$$

Here, $\bar{u}_{0,\mathrm{ref}}^{\mathrm{pl},n}$, $\bar{u}_{0,\mathrm{ref}}^{\mathrm{pl},t}$, $\bar{u}_{f,\mathrm{ref}}^{\mathrm{pl},n}$, $\bar{u}_{f,\mathrm{ref}}^{\mathrm{pl},t}$, α_2 and α_3 are parameters determined by the user, and the mode mixity angle θ is defined as

$$\theta=\arctan\left(\frac{f_n}{f_t}\right). \tag{A.17}$$

Eqs. (A.15) and (A.16) are super-ellipses that provide the normal-tangential interaction between $\bar{u}_0^{\mathrm{pl},n}$ and $\bar{u}_0^{\mathrm{pl},t}$ and between $\bar{u}_f^{\mathrm{pl},n}$ and $\bar{u}_f^{\mathrm{pl},t}$ in the plastic relative displacement plane.

The parameters that must be determined from experiments are thus E, R_n, R_t, β_1, α_1, $\bar{u}_{0,\mathrm{ref}}^{\mathrm{pl},n}$, $\bar{u}_{0,\mathrm{ref}}^{\mathrm{pl},t}$, $\bar{u}_{f,\mathrm{ref}}^{\mathrm{pl},n}$, $\bar{u}_{f,\mathrm{ref}}^{\mathrm{pl},t}$, β_2, β_3, α_2, α_3 and the radius of influence r, in addition to the hardening parameters R_0, Q_1 and θ_1. The parameters α_1, α_2 and α_3 were set to zero in this work.

List of Figures

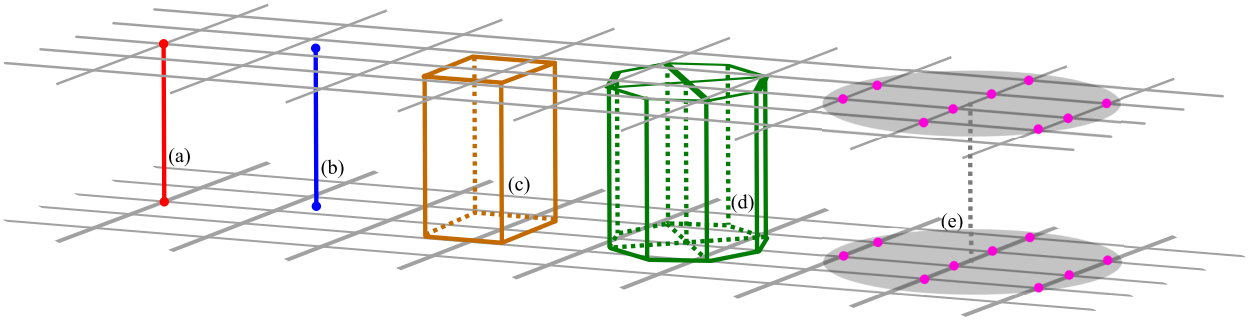

Fig. 1. Illustration of different connection modelling techniques. (a) rigid link. (b) beam element. (c) hexahedral element. (d) cluster of hexahedral elements. (e) constraint.

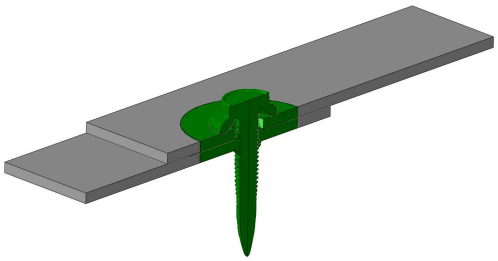

Fig. 2. Illustration of the definition of a *connection* (green).

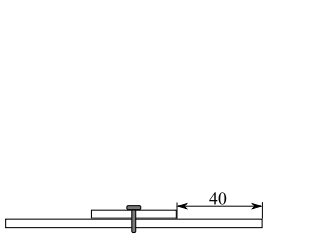

(a) Cross specimen.

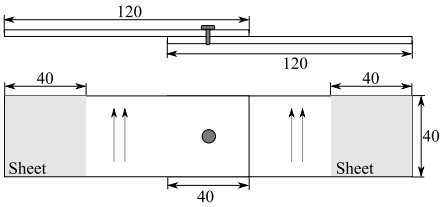

(b) Single lap joint specimen for the small screw connection.

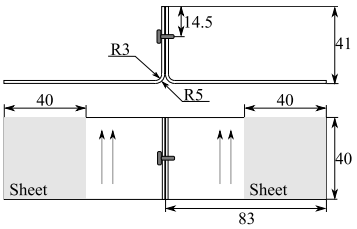

(c) Peeling specimen for the small screw connection.

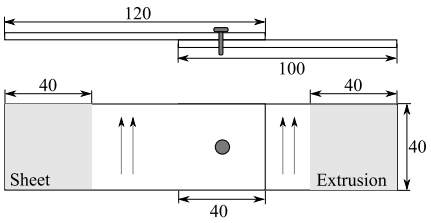

(d) Single lap joint specimen for the large screw connection.

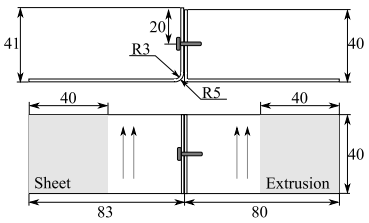

(e) Peeling specimen for the large screw connection.

Fig. 3. Single-connector test specimens. Arrows indicate the rolling/extrusion direction.

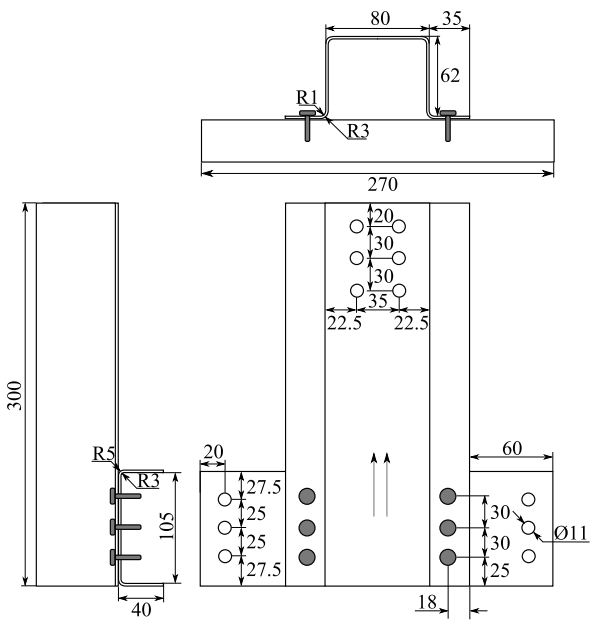

(a) T-component specimen for the small screw connection.

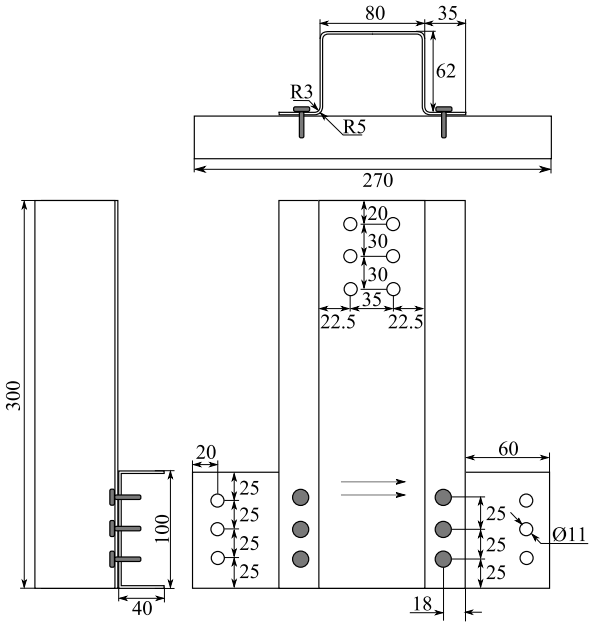

(b) T-component specimen for the large screw connection.

(c) Front of the test rig. Red rectangle shows the location of the DIC mesh (see Fig. 4e).

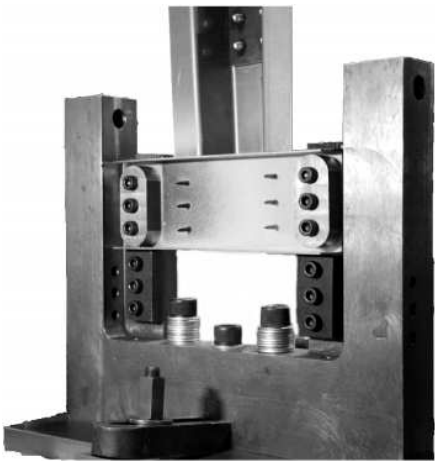

(d) Back of test rig.

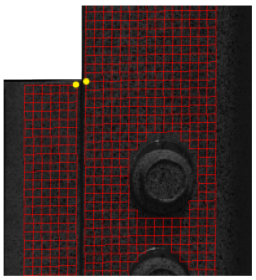

(e) DIC displacement measure (see Fig. 4c).

Fig. 4. Test set-up in T-component tests. Arrows indicate the rolling/extrusion direction. The nominal thickness is 2 mm.

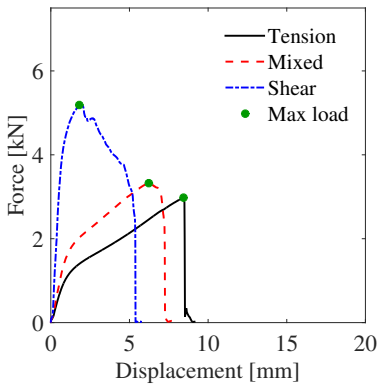

(a) Small screw connection (after Sønstabø et al. (2015)).

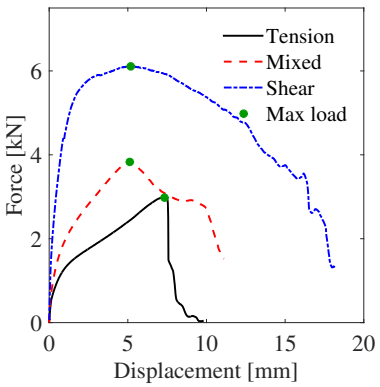

(b) Large screw connection.

Fig. 5. Representative curves from cross tests.

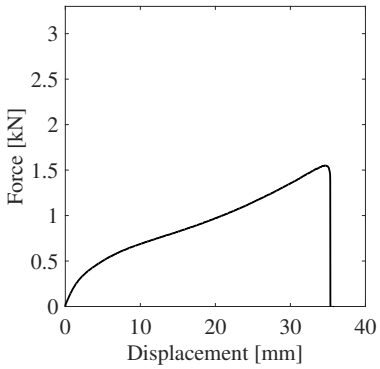

(a) Small screw connection (after Sønstabø et al. (2015)).

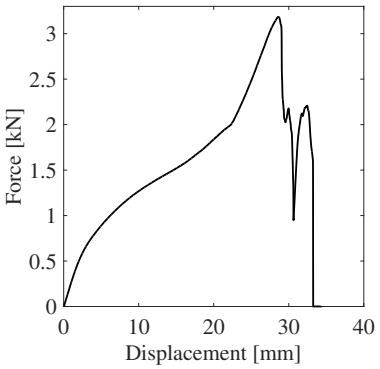

(b) Large screw connection.

Fig. 6. Representative curves from peeling tests.

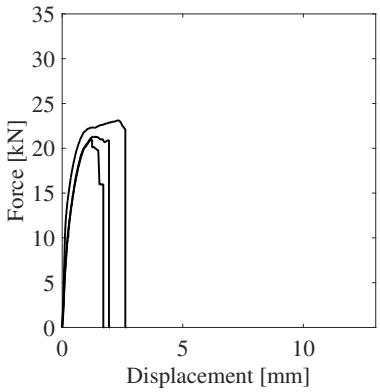

(a) Small screw connection.

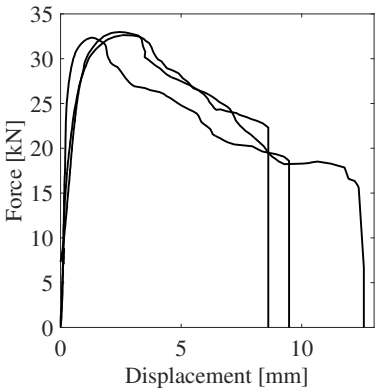

(b) Large screw connection.

Fig. 7. Curves from T-component tests.

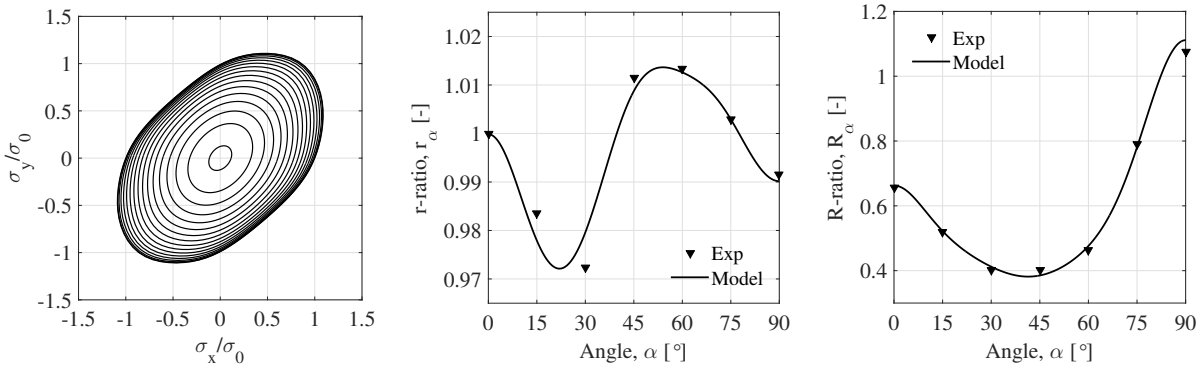

(a) Yield surface. (b) Experimental and computed *r*-values. (c) Experimental and computed *R*-values.

Fig. 8. Calibrated yield function compared to experimental data in the reference direction for AA 6016 T4.

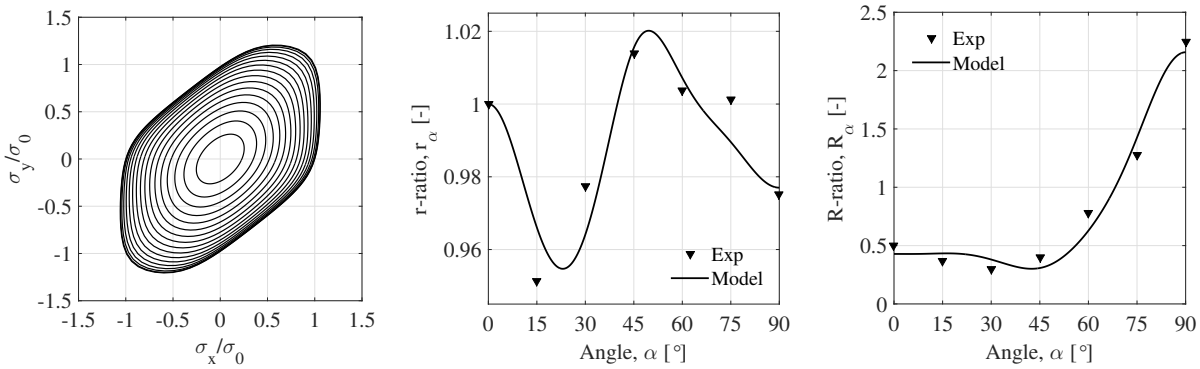

(a) Yield surface. (b) Experimental and computed *r*-values. (c) Experimental and computed *R*-values.

Fig. 9. Calibrated yield function compared to experimental data in the reference direction for AA 6063 T4.

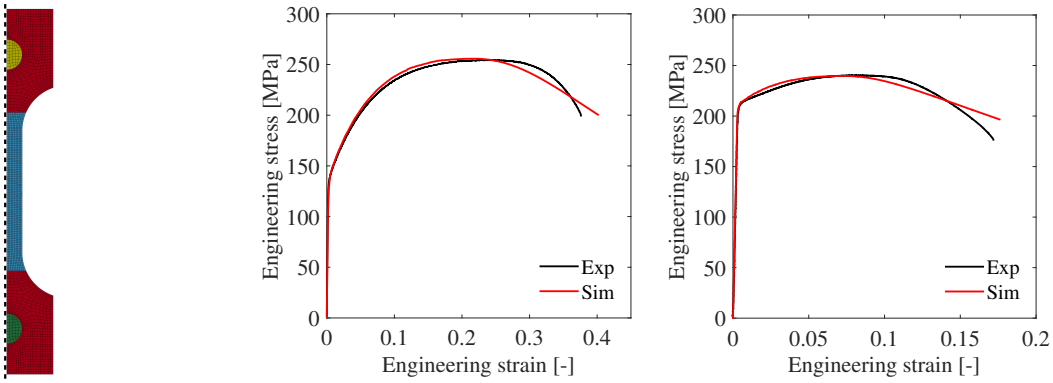

(a) FE model.

(b) Results for AA 6016 T4.

(c) Results for AA 6063 T6.

Fig. 10. FE model and results for uniaxial tensile test simulations in the reference direction after calibration of material model parameters.

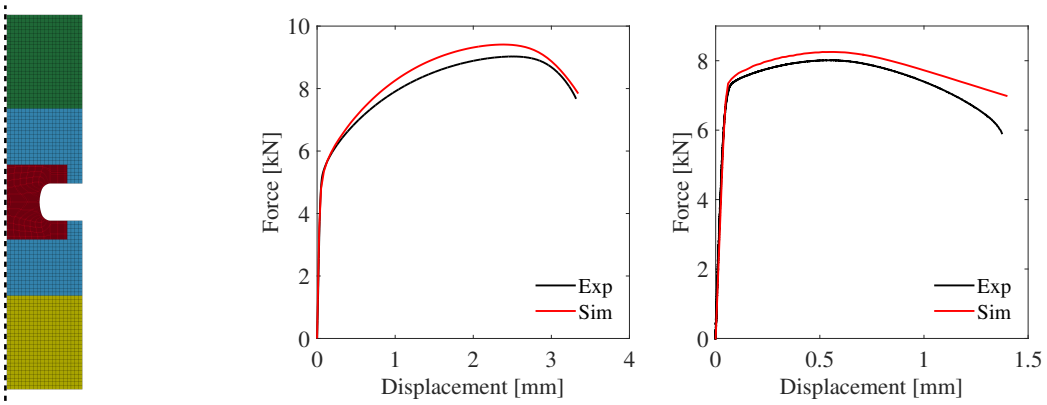

(a) FE model.

(b) Results for AA 6016 T4.

(c) Results for AA 6063 T6.

Fig. 11. FE model and results of simulations of plane strain tension tests.

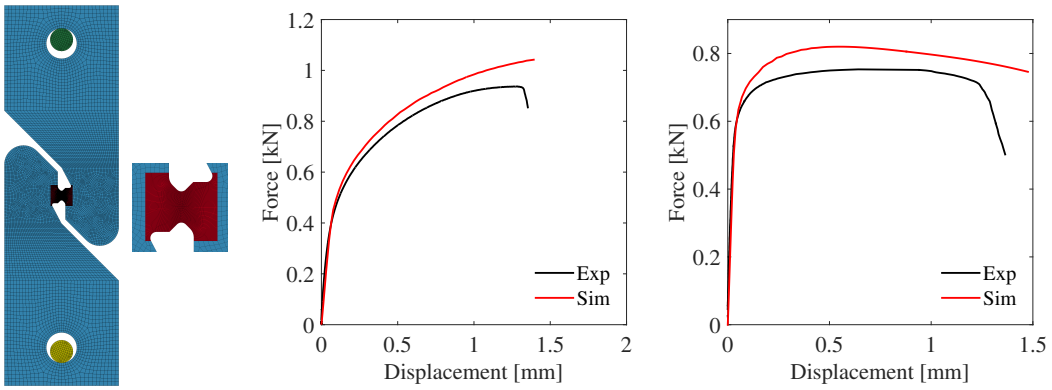

(a) FE model (central part enlarged).

(b) Results for AA 6016 T4.

(c) Results for AA 6063 T6.

Fig. 12. FE model and results of simulations of in-plane single shear tests.

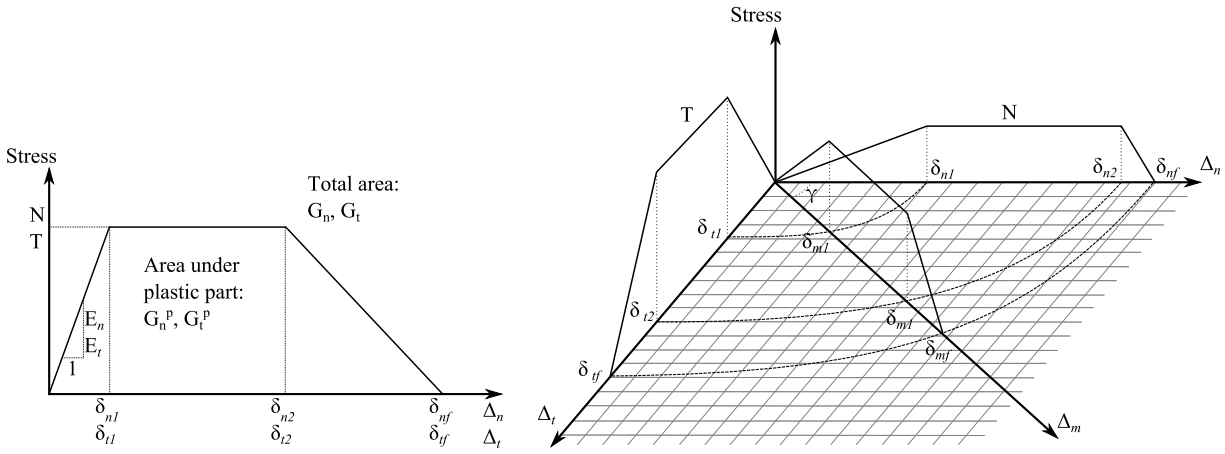

(a) Pure tensile and pure shear loading.

(b) Mixed mode.

Fig. 13. Tri-linear stress-separation curves for *element model 2*. See Appendix A.1 for descriptions of the parameters. After Marzi et al. (2009).

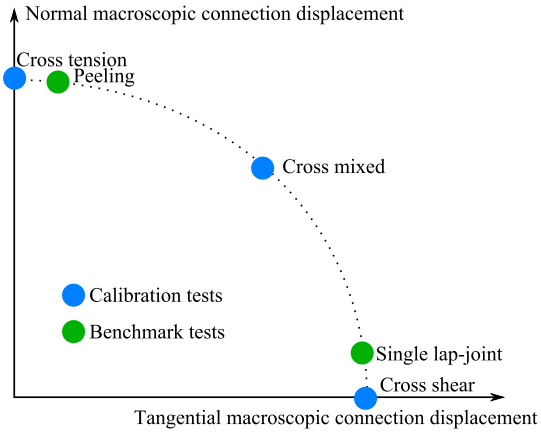

(a) General connection failure locus. The calibration tests are illustrated with blue dots, and the approximate assumed locations of the benchmark tests are indicated with green dots.

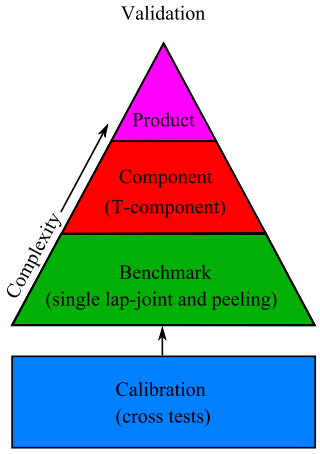

(b) Illustration of validation strategy.

Fig. 14. Illustrations explaining the calibration/validation procedure.

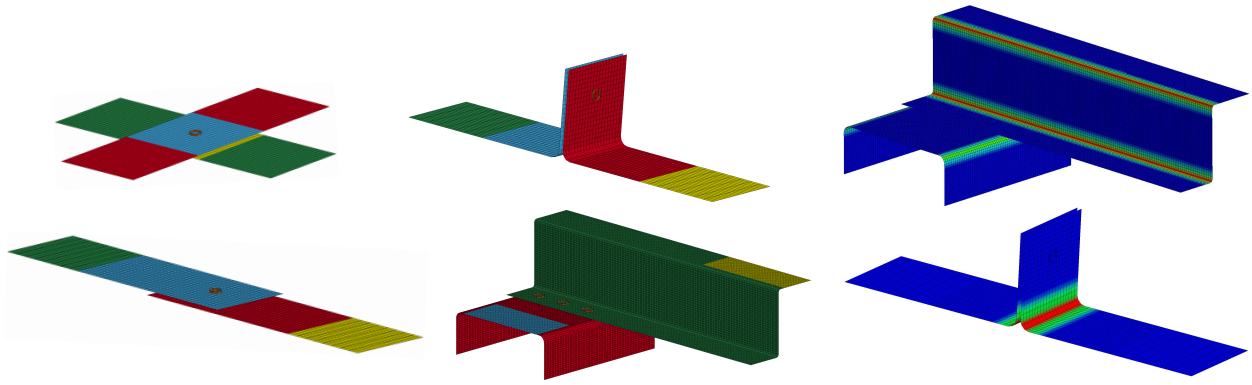

(a) FE models used for calibration and validation of the connection models: cross (top left), single lap joint (bottom left), peeling (top right) and T-component (bottom right).

(b) Fields of initial equivalent plastic strains in peeling and T-component models.

Fig. 15. FE models.

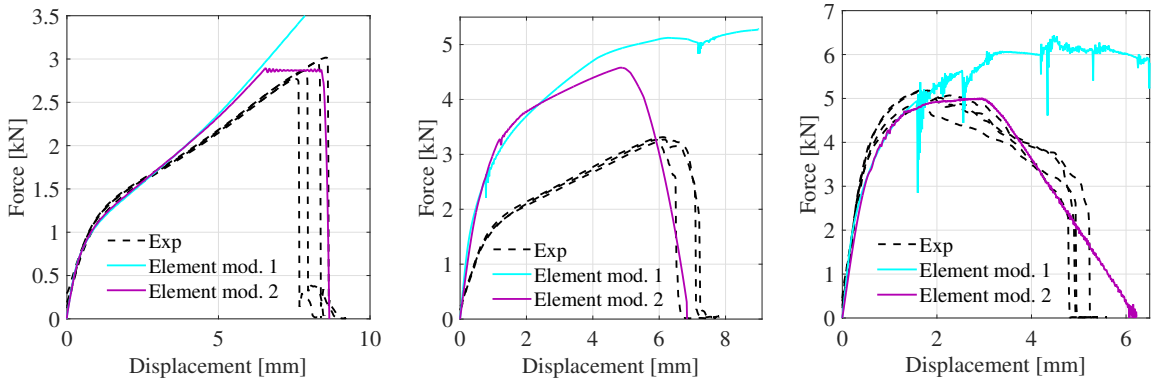

(a) Cross tension. (b) Cross mixed. (c) Cross shear.

Fig. 16. Results from the calibration of the element-based models to cross tests for the small screw connection.

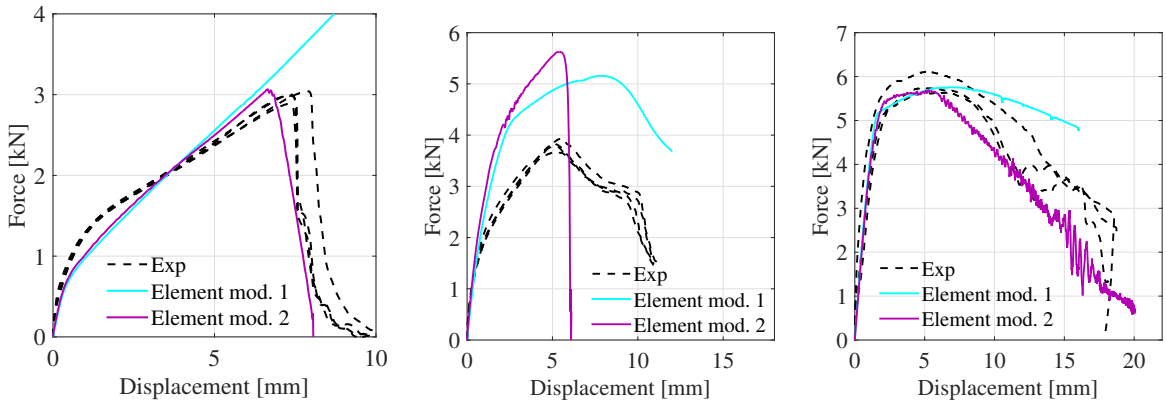

(a) Cross tension. (b) Cross mixed. (c) Cross shear.

Fig. 17. Results from the calibration of the element-based models to cross tests for the large screw connection.

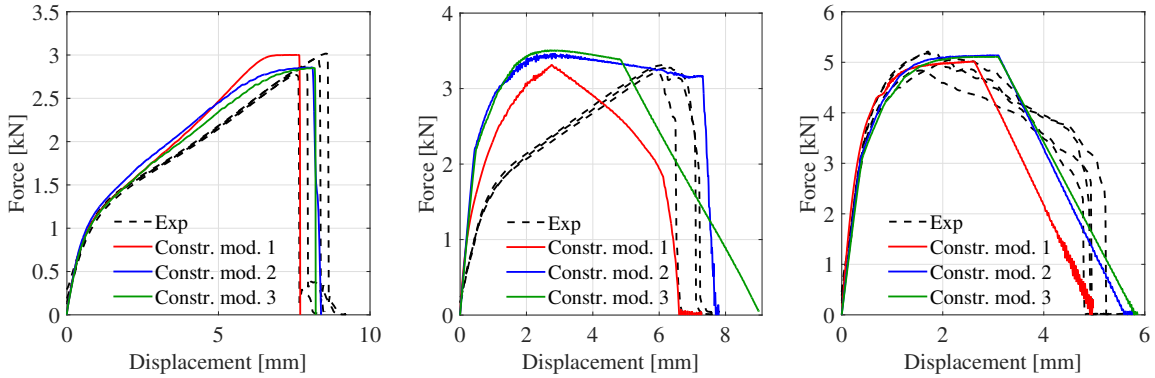

(a) Cross tension. (b) Cross mixed. (c) Cross shear.

Fig. 18. Results from the calibration of the constraint-based models to cross tests for the small screw connection.

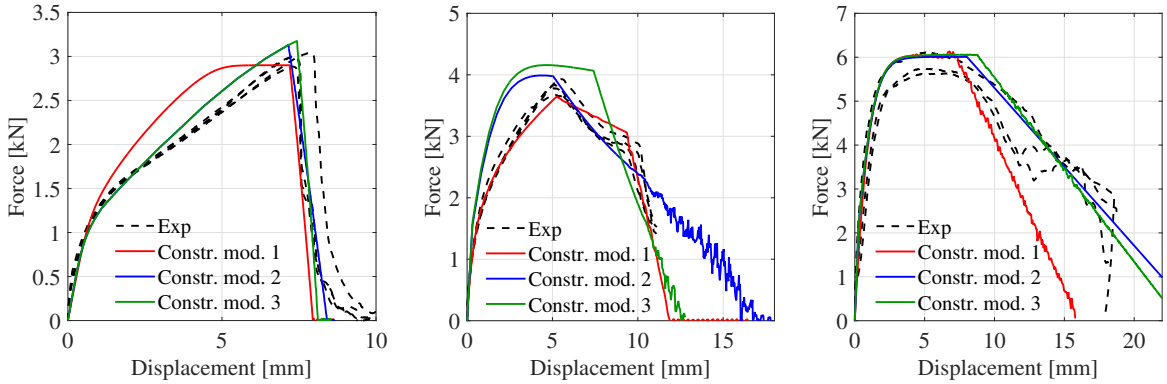

(a) Cross tension. (b) Cross mixed. (c) Cross shear.

Fig. 19. Results from the calibration of the constraint-based models to cross tests for the large screw connection.

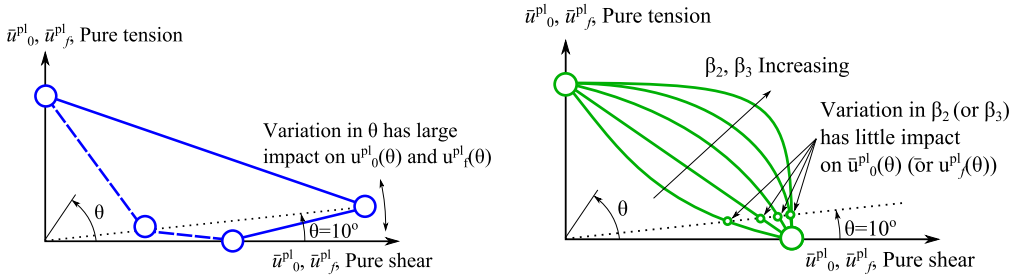

(a) *Constraint model 2*. Blue circles indicate the tabulated points, and the two lines indicate two possible interaction curves.

(b) *Constraint model 3*. Green circles represent the values in pure tension and pure shear.

Fig. 20. Conceptual illustrations of normal-tangential interaction curves for $\bar{u}^{pl}_0(\theta)$ and $\bar{u}^{pl}_f(\theta)$ to illustrate challenges with mode mixity angle θ defined by forces.

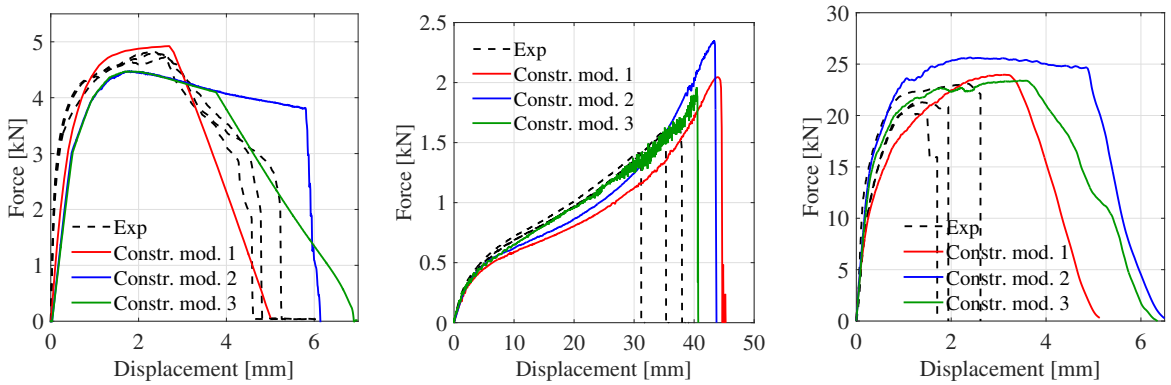

(a) Single lap joint. (b) Peeling. (c) T-component.

Fig. 21. Validation results for the small screw connection.

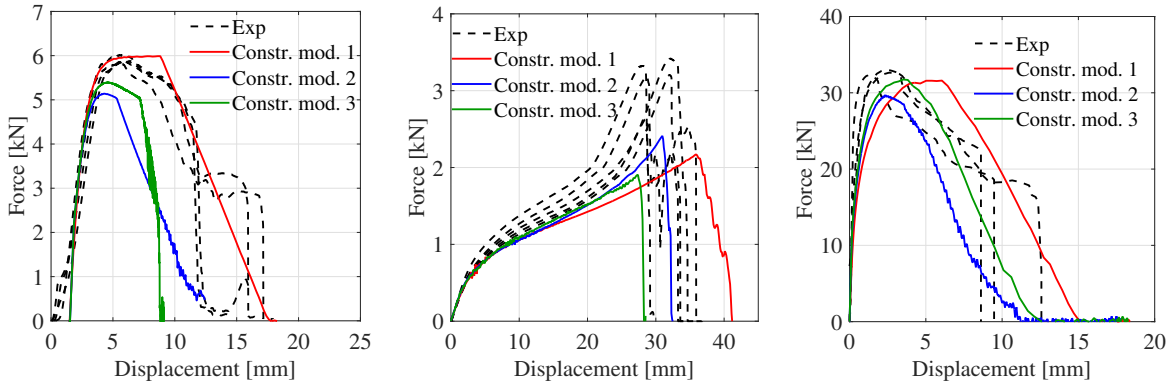

(a) Single lap joint. (b) Peeling. (c) T-component.

Fig. 22. Validation results for the large screw connection.

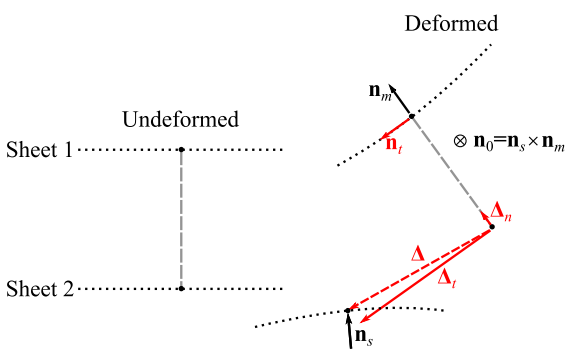

(a) *Constraint model 1*.

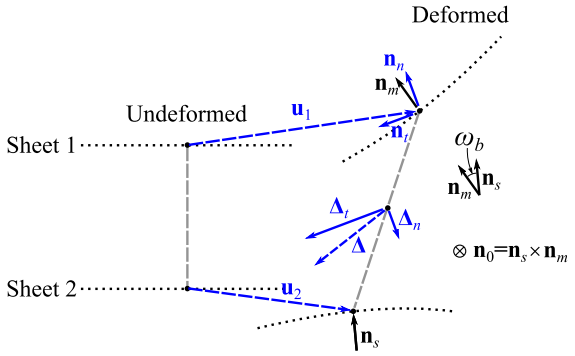

(b) *Constraint model 2* and *constraint model 3*.

Fig. 23. Illustration of kinematics of constraint-based models.

List of Tables

Table 1
Material model parameters for the base materials.

		6016 T4	6063 T6
σ_0	[MPa]	107.6	204.6
m	[-]	8.0	8.0
c'_{12}	[-]	-16.70	-1.51
c'_{13}	[-]	-6.69	-1.32
c'_{21}	[-]	18.56	0.82
c'_{23}	[-]	12.34	-0.19
c'_{31}	[-]	9.23	2.29
c'_{32}	[-]	-9.68	2.18
c'_{44}	[-]	0.70	0.55
c'_{55}	[-]	1.00	1.00
c'_{66}	[-]	1.00	1.00
c''_{12}	[-]	-17.46	0.93
c''_{13}	[-]	-7.22	-0.47
c''_{21}	[-]	11.26	-0.71
c''_{23}	[-]	12.34	-0.92
c''_{31}	[-]	7.49	0.39
c''_{32}	[-]	-11.15	1.62
c''_{44}	[-]	0.99	1.06
c''_{55}	[-]	1.00	1.00
c''_{66}	[-]	1.00	1.00
Q_{R1}	[MPa]	29.2	8.0
θ_{R1}	[MPa]	25000	12300
Q_{R2}	[MPa]	149.5	55.0
θ_{R2}	[MPa]	2011	1472.6
Q_{R3}	[MPa]	100	
θ_{R3}	[MPa]	230.8	

Table 2
Overview of element model 1 and constraint models 1, 2 and 3, showing the important differences. All models and their parameters are presented in detail in Appendix A.

	Element model 2	Constraint model 1	Constraint model 2	Constraint model 3
Kinematics	Separations calculated from element's relative displacements: $\Delta_n = \max(u_n, 0)$ $\Delta_t = \sqrt{u_{t1}^2 + u_{t2}^2}$ $\Delta_m = \sqrt{\Delta_n^2 + \Delta_t^2}$	Total stretch $\boldsymbol{\Delta}$ defined as the vector between the slave end and its original location on the deformed slave sheet. Normal and tangential stretch: $\Delta_n = \lvert\boldsymbol{\Delta}\cdot\mathbf{n}_m\rvert, \quad \Delta_t = \lvert\boldsymbol{\Delta}\cdot\mathbf{n}_t\rvert$ $\mathbf{n}_t = \mathbf{n}_0 \times \mathbf{n}_m$	Total stretch defined as the relative displacement between the two sheets: $\boldsymbol{\Delta} = \mathbf{u}_2 - \mathbf{u}_1$ Normal and tangential stretch: $\Delta_n = \lvert\boldsymbol{\Delta}\cdot\mathbf{n}_n\rvert, \quad \Delta_t = \lvert\boldsymbol{\Delta}\cdot\mathbf{n}_t\rvert$ $\mathbf{n}_n = \frac{\mathbf{n}_m + \mathbf{n}_s}{\lvert\mathbf{n}_m + \mathbf{n}_s\rvert}, \quad \mathbf{n}_t = \mathbf{n}_0 \times \mathbf{n}_n$ Relative rotation between sheets: $\omega_b = \arccos \frac{\mathbf{n}_s \cdot \mathbf{n}_m}{\lvert\mathbf{n}_s\rvert\,\lvert\mathbf{n}_m\rvert}$	
Mode mixity	$\theta = \arccos \frac{\langle u_n \rangle}{\Delta_m}$	$\theta = \arctan\left(\frac{\Delta_n}{\Delta_t}\right)$	$\theta = \arctan\left(\frac{F_n}{F_t}\right)$ $F_n = f_n + \alpha m_b$ $F_t = f_t$	$F_n = f_n$ $F_t = f_t$
Elasticity	$\tilde{\boldsymbol{\sigma}} = \boldsymbol{E}\boldsymbol{u}^e$ $\tilde{\boldsymbol{\sigma}} = [\tilde{\sigma}_n, \tilde{\sigma}_{t1}, \tilde{\sigma}_{t2}]^\mathsf{T}$ $\boldsymbol{u}^e = \left[u_n^e, u_{t1}^e, u_{t2}^e\right]^\mathsf{T}$ $\boldsymbol{E} = \begin{bmatrix} E_n & 0 & 0 \\ 0 & E_t & 0 \\ 0 & 0 & E_t \end{bmatrix}$	Forces are calculated directly from mathematical expressions: $f_n = \frac{f_n^{\max}\Delta_n}{\eta_{\max}\Delta_n^{\text{fail}}}\hat{f}_n$ $f_t = \frac{f_t^{\max}\Delta_t}{\eta_{\max}\Delta_t^{\text{fail}}}\hat{f}_t,$ where $\hat{f}_n = 1 - \left(\frac{\xi_n - \eta_{\max}}{\xi_n}\right)^8$ $\hat{f}_t = 1 - \left(\frac{\xi_t - \eta_{\max}}{\xi_t}\right)^8$	$\tilde{\boldsymbol{f}} = \boldsymbol{E}\boldsymbol{u}$ $\tilde{\boldsymbol{f}} = [f_n, f_t, m_b]$ $\boldsymbol{u} = [\Delta_n, \Delta_t, \omega_b]$	$\tilde{\boldsymbol{f}} = [f_n, f_t]$ $\boldsymbol{u} = [\Delta_n, \Delta_t]$
Plasticity	Uncoupled perfect plasticity in normal and tangential directions.		Yield surface: $\left[\left(\frac{F_n}{F_n^c}\right)^{\beta_1} + \left(\frac{F_t}{F_t^c}\right)^{\beta_1}\right]^{\frac{1}{\beta_1}} - F_0 = 0$ $F_n = f_n + \alpha_1 m_b$ $F_t = f_t$ $F_n^c = R_n$ $F_t^c = R_t$	$F_n = f_n$ $F_t = f_t$ $F_n^c = R_n(1 - \alpha_1\omega_b)$ $F_t^c = R_t$
Damage	Damage variable: $d = \frac{\Delta_m - \delta_{m2}}{\delta_{mf} - \delta_{m2}}$ Stresses scaled by damage variable: $\boldsymbol{\sigma} = (1 - d)\tilde{\boldsymbol{\sigma}}$	Damage variables: $d_n = \frac{\eta_{\max} - \xi_n}{1 - \xi_n}, \quad d_t = \frac{\eta_{\max} - \xi_t}{1 - \xi_t}$ When $\eta_{\max} \geq \xi_n$ and/or $\eta_{\max} \geq \xi_t$, forces are scaled by damage variables: $f_n = \frac{f_n^{\max}\Delta_n}{\eta_{\max}\Delta_n^{\text{fail}}}(1 - d_n)$ $f_t = \frac{f_t^{\max}\Delta_t}{\eta_{\max}\Delta_t^{\text{fail}}}(1 - d_t)$	Damage variable: $d = \frac{\bar{u}^{\text{pl}} - \bar{u}_0^{\text{pl}}(\theta)}{\bar{u}_f^{\text{pl}}(\theta)}$ $\bar{u}_0^{\text{pl}}(\theta)$ and $\bar{u}_f^{\text{pl}}(\theta)$ are functions tabulated by the user. Forces scaled by damage variable: $\boldsymbol{f} = (1 - d)\,\tilde{\boldsymbol{f}}$	$\bar{u}_0^{\text{pl}}(\theta)$ and $\bar{u}_f^{\text{pl}}(\theta)$ are defined by mathematical expressions (Eqs. (A.15) and (A.16)).

Table 3
Parameters of the element-based models obtained for the two connections, including descriptions.

	Parameter	Description	The small screw connection	The large screw connection
Element model 1		Number of elements in connection	16	16
	D	Diameter of cluster of elements	1.5 mm	3.0 mm
	E	Young's modulus	4000 MPa	2000 MPa
	ν	Poisson's ratio	0.3	0.3
	σ_y	Yield stress	700 MPa	725 MPa
	H	Hardening modulus	0 MPa	300 MPa
Element model 2		Number of elements in connection	4	4
	D	Diameter of cluster of elements	3.0 mm	3.5 mm
	E	Elastic stiffness in tension	5000 N/mm	5000 N/mm
	N	Yield stress in tension	345.9 MPa	265 MPa
	G_n	Total area under traction-separation curve in tension	888.3 N/mm	400 N/mm
	f_{Gn}	Fraction of total area that is plastic in tension	0.834	0.325
	G	Elastic stiffness in shear	2703.9 N/mm	1000 N/mm
	T	Yield stress in shear	809.2 MPa	681.8 MPa
	G_t	Total area under traction-separation curve in shear	2856 N/mm	23800 N/mm
	f_{Gn}	Fraction of total area that is plastic in shear	0.496	0.19

Table 4
Parameters of the constraint-based models obtained for the two connections, including descriptions.

	Parameter	Description	The small screw connection	The large screw connection
Constraint model 1	r	Radius of influence	3.0 mm	6.0 mm
	$f_n^{\max}$	Maximum pure normal force	3000 N	2900 N
	$f_t^{\max}$	Maximum pure shear force	5000 N	6000 N
	Δ_n^{fail}	Deformation at failure for pure normal deformation	2.0 mm	5.2 mm
	Δ_t^{fail}	Deformation at failure for pure shear deformation	4.8 mm	16.0 mm
	ξ_n	Fraction of Δ_n where softening starts in pure normal deformation	0.9	0.72
	ξ_t	Fraction of Δ_t where softening starts in pure shear deformation	0.5	0.45
	α_1	Parameter to control influence of mode mixity on η	0.05	0.34
	α_2	Parameter to control influence of mode mixity on η	0.65	0.89
	α_3	Parameter to control influence of mode mixity on η	1.4	1.25
Constraint model 2	E	Elastic stiffness	9800 N/mm	9000 N/mm
	r	Radius of influence	4.3 mm	5.0 mm
	R_n	Load capacity in normal direction	2504 N	2509 N
	R_t	Load capacity in shear direction	4467 N	4360 N
	β_1	Exponent controlling shape of force interaction curve	1.3	1.25
	R_0	User parameter in hardening term (defined by authors)	0.692765	0.50829
	Q_1	User parameter in hardening term (defined by authors)	0.45	0.87
	θ_1	User parameter in hardening term (defined by authors)	0.000358 [$N^{-1}mm^{-1}$]	0.000325 [$N^{-1}mm^{-1}$]
	$\bar{u}_0^{\text{pl}}(90°)$	Plastic relative damage initiation displacement in tension	6656 Nmm	5078 Nmm
	$\bar{u}_0^{\text{pl}}(10°)$	Plastic relative damage initiation displacement in mixed loading	16182 Nmm	10485 Nmm
	$\bar{u}_0^{\text{pl}}(0°)$	Plastic relative damage initiation displacement in shear	9857 Nmm	31472 Nmm
	$\bar{u}_f^{\text{pl}}(90°)$	Plastic relative failure displacement in tension	2144 Nmm	4845 Nmm
	$\bar{u}_f^{\text{pl}}(10°)$	Plastic relative failure displacement in mixed loading	1228 Nmm	25889 Nmm
	$\bar{u}_f^{\text{pl}}(0°)$	Plastic relative failure displacement in shear	11506 Nmm	73277 Nmm
Constraint model 3	E	Elastic stiffness	9000 N/mm	9000 N/mm
	r	Radius of influence	3.2 mm	5.0 mm
	R_n	Load capacity in normal direction	2504 N	2509 N
	R_t	Load capacity in shear direction	4467 N	4360 N
	β_1	Exponent controlling shape of force interaction curve	1.3	1.4
	R_0	User parameter in hardening term (defined by authors)	0.692765	0.50829
	Q_1	User parameter in hardening term (defined by authors)	0.45	0.87
	θ_1	User parameter in hardening term (defined by authors)	0.000358 $N^{-1}mm^{-1}$	0.000325 $N^{-1}mm^{-1}$
	$\bar{u}_{0,t}^{\text{pl}}$	Plastic relative damage initiation displacement in tension	5808 Nmm	5520 Nmm
	$\bar{u}_{0,s}^{\text{pl}}$	Plastic relative damage initiation displacement in shear	8711 Nmm	34640 Nmm
	β_2	Exponent controlling shape of damage initiation interaction curve	2.0	2.0
	$\bar{u}_{f,t}^{\text{pl}}$	Plastic relative failure displacement in tension	6000 Nmm	8921 Nmm
	$\bar{u}_{f,s}^{\text{pl}}$	Plastic relative failure displacement in shear	21251 Nmm	98076 Nmm
	β_3	Exponent controlling shape of failure interaction curve	10.1	1.546